Supporting Information

Copper(I) complexes based on ligand systems with two different binding sites: Synthesis, structures and reaction with O_2

S. T. Li, B. Braun-Cula, S. Hoof and C. Limberg

1. Crystallographic Data

Crystal structure determination. Crystal data and parameters are shown in Table S1 and Table S2. All data collections were performed with a STOE IPDS 2 T diffractometer (for complex **2**) or a BRUKER D8 VENTURE diffractometer at 100 K, using Mo-Kα radiation (λ = 0.71073 Å). The structures were solved by direct methods using SHELXS-97 and refined by full matrix least squares procedures based on F^2 with all measured reflections with SHELXL-2013.[1] Multi-scan corrections were applied to the data.[2] All non-hydrogen atoms were refined anisotropically. All hydrogen atom positions were introduced at their idealized positions and were refined using a riding model.

CCDC 1566560 (for **1**·0.5(CH_3CN)), 1566561 (for **2**), 1566562 (for **3**), 1566563 (for **4**), 1566564 (for **6**·$C_4H_{10}O$), 1566565 for (**7**·($C_4H_{10}O$)(C_3H_6O)), 1566566 (for **9**), 1566567 (for **11**) and 1566568 (for $\mathbf{L^1}$) contain the supplementary crystallographic data for this paper. These data can be obtained free of charge from the Cambridge Crystallographic Data Centre via www.ccdc.cam.ac.uk/data_request/cif.

Table S1. Crystal data and experimental parameters for the crystal structure analyses of $\mathbf{L^1}$, **1**·0.5(CH_3CN), **2**, **3** and **4**.

	$\mathbf{L^1}$	**1**·0.5(CH_3CN)	**2**	**3**	**4**
Formula	$C_{36}H_{44}N_6O$	$C_{37}H_{45.5}Cl_2Cu_2N_{6.5}O$	$C_{72}H_{88}Br_6Cu_6N_{12}O_2$	$C_{72}H_{88}Cu_6I_6N_{12}O_2$	$C_{40}H_{50}B_2Cu_2F_8N_8O$
Formula weight	576.77	795.28	2014.24	2296.18	959.58
Crystal system	triclinic	monoclinic	triclinic	triclinic	monoclinic
Space group	*P*-1	$P2_1/n$	*P*-1	*P*-1	$P2_1/c$
a /Å	10.107(6)	15.9214 (9)	9.3339 (4)	9.4577 (11)	10.5665 (7)
b /Å	11.960 (7)	14.9212 (9)	12.9707 (6)	13.2450 (16)	30.175 (2)
c /Å	14.061 (12)	16.2057 (10)	15.5982 (7)	16.0086 (19)	14.7838 (10)
α /°	82.27 (4)	90	94.999 (4)	95.888 (4)	90
β /°	72.09 (3)	112.376 (2)	103.629 (4)	103.463 (5)	99.611 (2)
γ /°	74.94 (2)	90	91.613 (4)	91.098 (5)	90
V /Å^3	1559.0(18)	3560.1 (4)	1825.96 (14)	1938.0 (4)	4647.6 (5)
Z	2	4	1	1	4
D(calc.) /g·cm^{-3}	1.229	1.484	1.832	1.967	1.371
μ(Mo-K$_\alpha$) /mm^{-1}	0.076	1.385	5.053	4.058	0.987
θ range /°	2.177 to 25.329	2.279 to 36.395	3.157-25.617	2.295-26.407	2.306-30.019
Rflns collected	28227	118566	22251	78607	112997
Independent rflns	5659	17330	6837	7928	12238
F(000)	620	1652	1004	1112	1976
GOF on F^2	1.075	1.021	1.061	1.044	1.100
R_1 ($I_0 > 2\sigma(I)$)	0.0362	0.0442	0.0279	0.0219	0.0879
wR_2 (all data)	0.0872	0.0932	0.0516	0.0590	0.2042
Peak and hole/ e·Å^{-3}	0.243/-0.211	1.759/-0.794	0.515/-0.446	1.135/-0.543	1.732/-0.847

Table S2. Crystal data and experimental parameters for the crystal structure analyses of **6**·($C_4H_{10}O$), **7**·($C_4H_{10}O$)(C_3H_6O), **9** and **11**.

	6·($C_4H_{10}O$)	**7**·($C_4H_{10}O$)(C_3H_6O)	**9**	**11**
Formula	$C_{42}H_{57}Cl_2Cu_2N_7O_{10}$	$C_{69}H_{84}Cu_2F_{12}N_6O_3P_4$	$C_{41}H_{52}Cu_2F_{12}N_8OP_2$	$C_{63}H_{70}Cu_2F_{12}N_6OP_4$
Formula weight	1017.92	1524.38	1089.92	1406.21
Crystal system	orthorhombic	triclinic	monoclinic	triclinic
Space group	*P*bca	*P*-1	*P*2/n	*P*-1
a /Å	16.6002 (7)	15.353 (8)	14.2462 (9)	12.5918 (10)
b /Å	17.2054 (7)	15.932 (6)	9.2140 (5)	12.9671 (10)
c /Å	31.5780 (17)	16.247 (7)	35.166 (2)	20.7089 (17)
α /°	90	98.83 (5)	90	86.642 (3)
β /°	90	115.99 (4)	95.872 (2)	84.270 (3)
γ /°	90	93.96 (5)	90	82.811 (3)
V /Å^3	9019.1 (7)	3488 (3)	4591.8 (5)	3334.3 (5)
Z	8	2	4	2
D(calc.) /g · cm^{-3}	1.499	1.452	1.577	1.401
μ(Mo-K$_\alpha$) /mm^{-1}	1.126	0.784	1.088	0.812
θ range /°	2.367 to 25.430	2.490 to 26.198	2.210-25.388	2.138-25.437
Rflns collected	109894	100200	85974	74965
Independent rflns	8296	13829	8436	12277
F(000)	4240	1580	2232	1448
GOF on F^2	1.046	1.016	1.031	1.080
R_1 ($I_0 > 2\sigma(I)$)	0.0458	0.0524	0.0347	0.0453
wR_2 (all data)	0.1151	0.1268	0.0732	0.1176
Peak and hole/ e·Å^{-3}	1.187/–1.425	1.641/–1.415	0.561/-0.335	1.679/-1.421

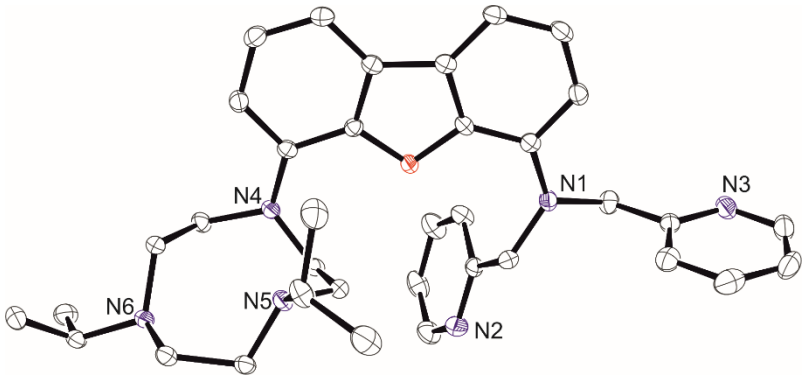

Figure S1. Molecular structure of **L^1**. Hydrogen atoms are omitted for clarity. Selected bond lengths [Å] und angles [°]: N1–C13 1.3930(18), N1–C6 1.4609(18), N1–C7 1.4520(19), N2–C1 1.3474(19), N2–C5 1.3458(18), N3–C8 1.3462(19), N3–C12 1.344(2), N4–C24 1.3937(17), N4–C36 1.4661(17), N4–C25 1.4737(18), N5–C26 1.459(2), N5–C30 1.4704(18), N6–C31 1.4661(18), N6–C35 1.4799(17), C13-N1-C6 124.18(11), C13-N1-C7 119.26(12), C1-N2-C5 116.89(13), C8-N3-C12 116.95(13), C24-N4-C25 121.29(10), C24-N4-C36 118.03(11), C26-N5-C30 112.90(10), C31-N6-C35 114.45(10).

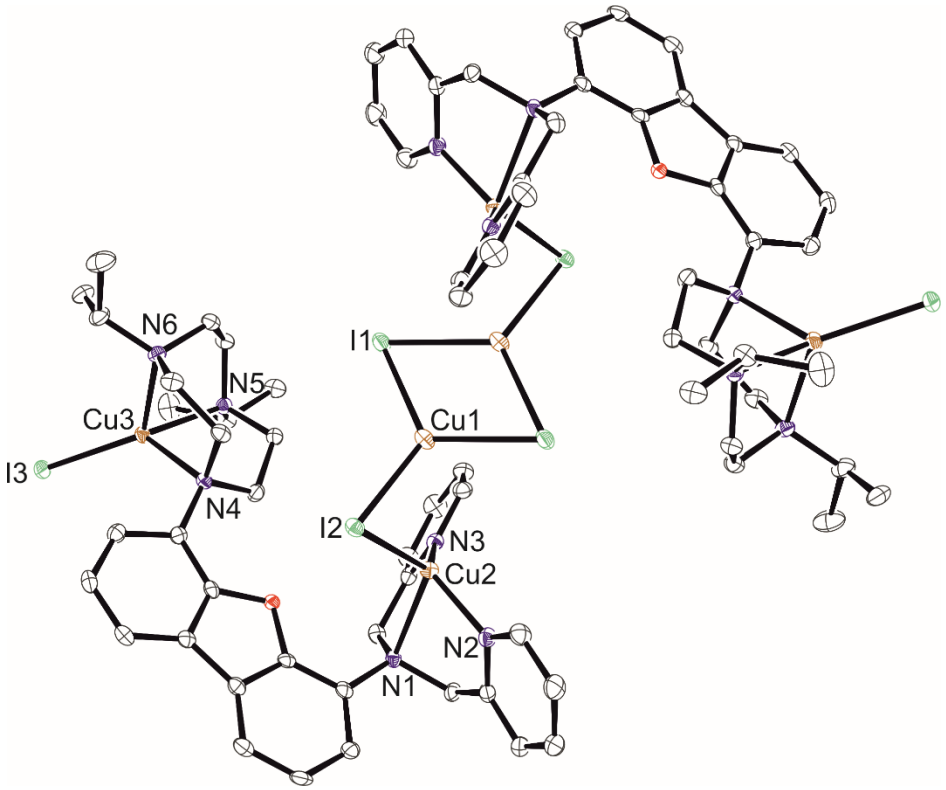

Figure S2. Molecular structure of **3**. Hydrogen atoms are omitted for clarity. Selected bond lengths [Å] and angles [°]: Cu2···Cu3 7.4196(10), Cu2–N1 2.359(2), Cu2–N2 2.028(2), Cu2–N3 1.987(2), Cu2–I2 2.5509(4), Cu3–N4 2.211(2), Cu3–N5 2.160(2), Cu3–N6 2.191(2), Cu3–I3 2.4661(4), N1-Cu2-N2 79.38(8), N1-Cu2-N3 79.52(8), N1-Cu2-I2 115.36(5), N2-Cu2-N3 122.92(8), N2-Cu2-I2 109.19(6), N3-Cu2-I2 127.79(6), N4-Cu3-N5 85.47(7), N4-Cu3-N6 84.05(8), N4-Cu3-I3 125.98(5), N5-Cu3-N6 84.34(8), N5-Cu3-I3 137.18(6), N6-Cu3-I3 122.92(5).

2. NMR spectra

Ligands

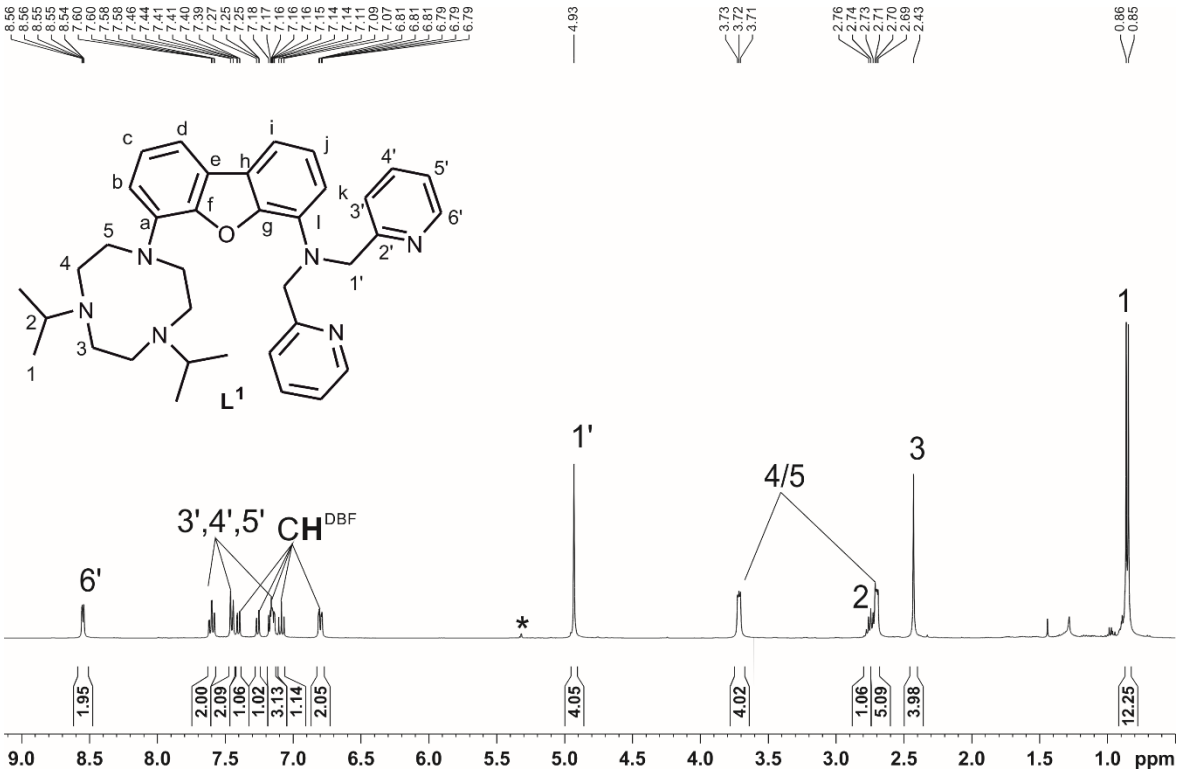

Figure S3. ^{1}H NMR (400.1 MHz, 297 K) specrtum of **L^{1}** in CD_2Cl_2.

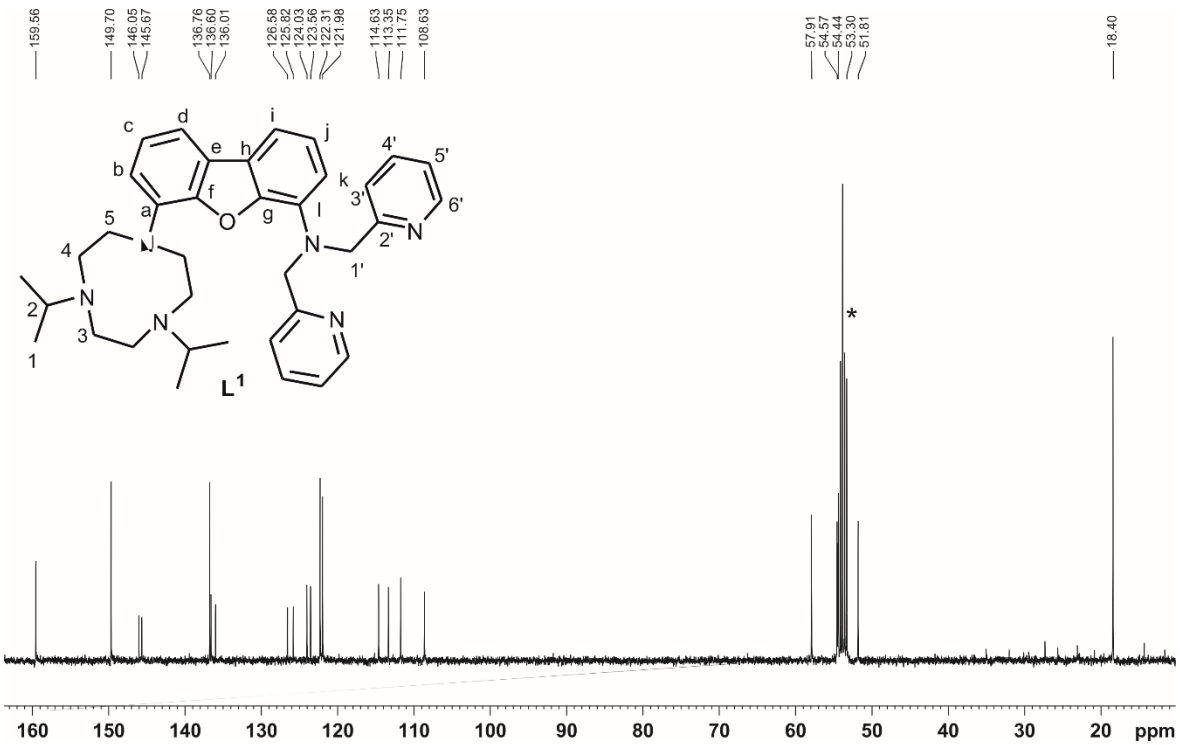

Figure S4. ^{13}C NMR (100.6 MHz, 297 K) spectrum of **L^{1}** in CD_2Cl_2.

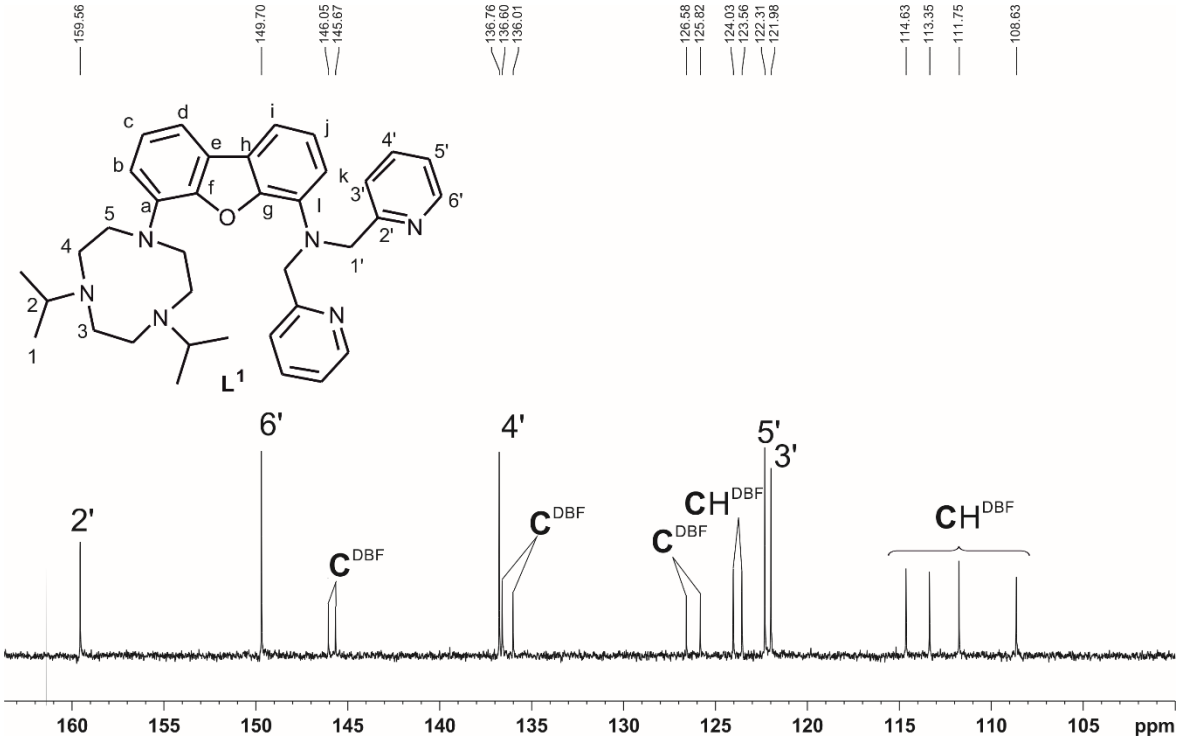

Figure S5. Magnified section of the ^{13}C NMR (100.6 MHz, 297 K) spectrum of $\mathbf{L^1}$ in CD_2Cl_2 showing the quaternary and aromatic C-atoms in the region 165-100 ppm. Quartenary and aromatic C-atoms of the dibenzofuran backbone that could not been clearly assigned were marked as $\mathbf{C}^{DBF}$ and $\mathbf{C}H^{DBF}$.

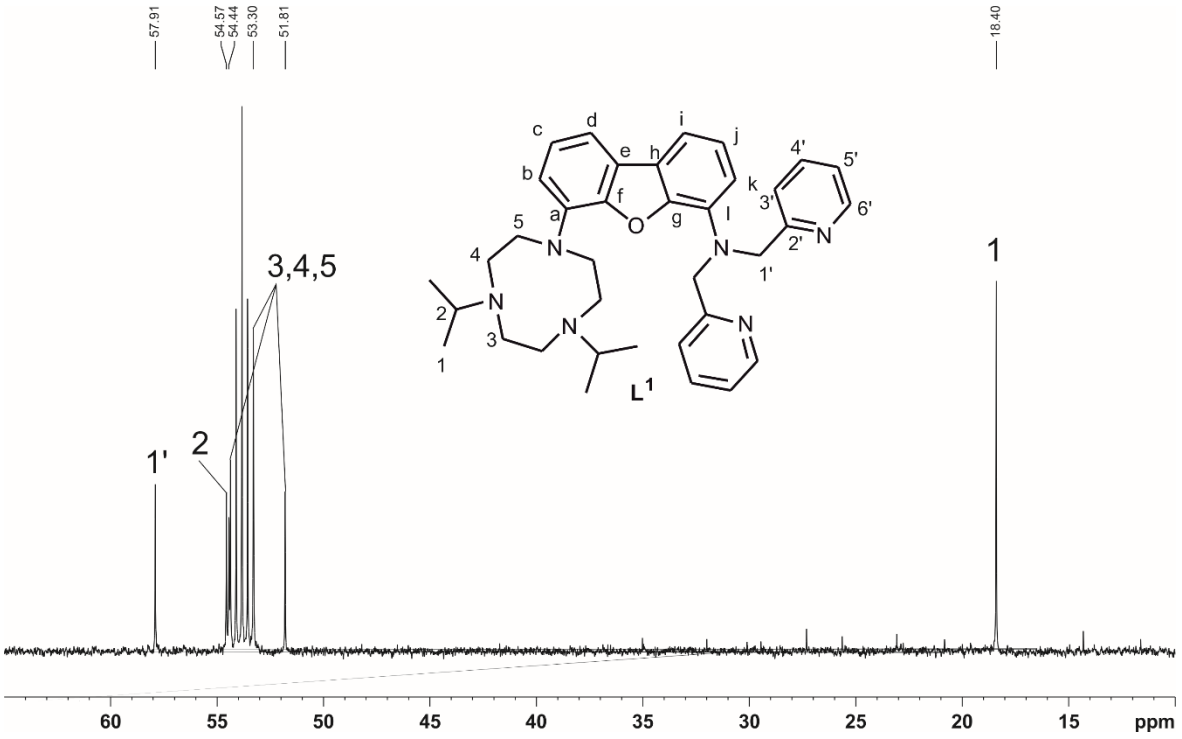

Figure S6. Magnified section of the ^{13}C NMR (100.6 MHz, 297 K) spectrum of $\mathbf{L^1}$ in CD_2Cl_2 in the region 65-10 ppm.

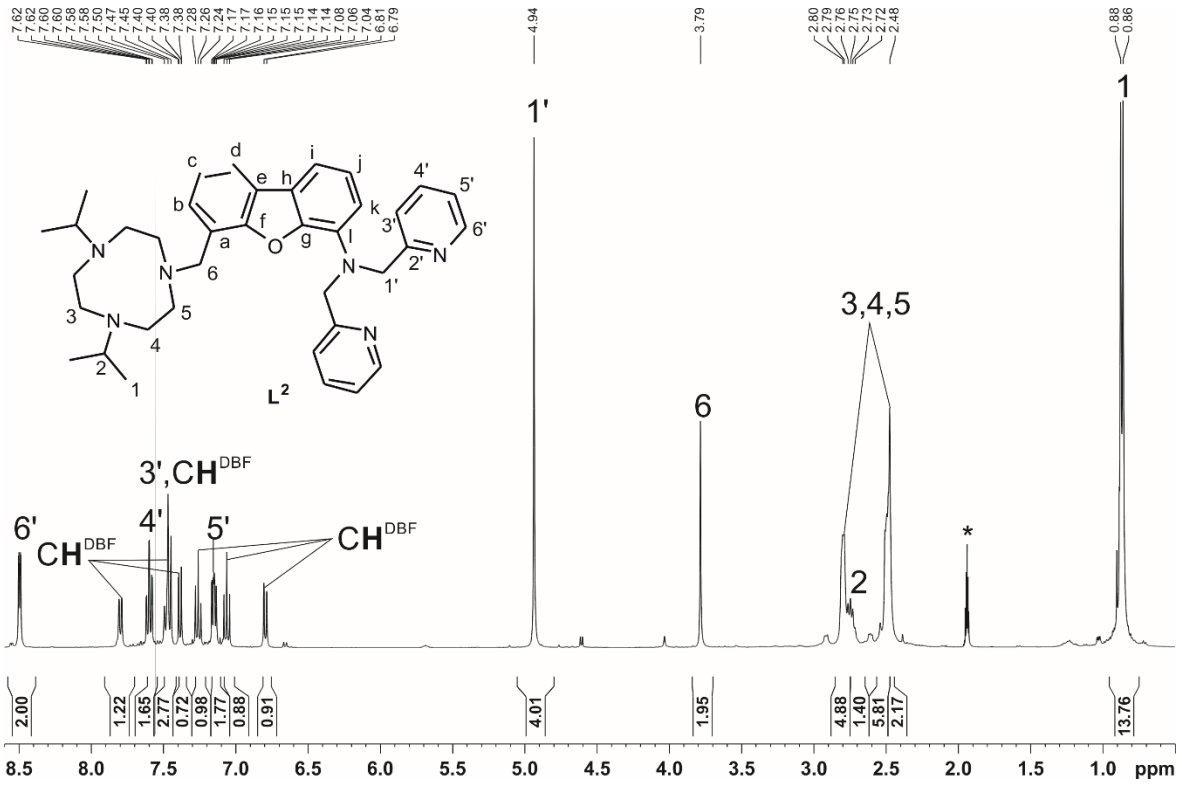

Figure S7. ^{1}H NMR (400.1 MHz, 297 K) spectrum of $\mathbf{L^2}$ in CD_3CN.

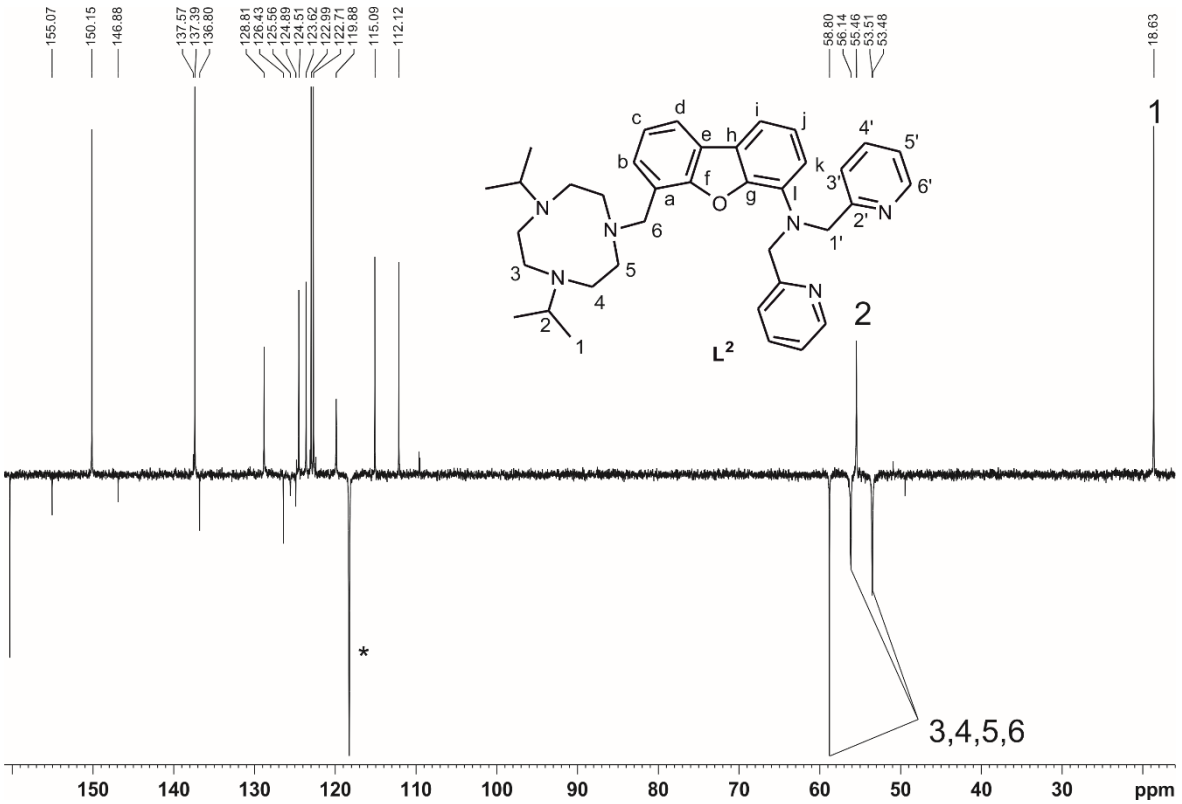

Figure S8. ^{13}C APT NMR (100.6 MHz, 297 K) spectrum of $\mathbf{L^2}$ in CD_3CN.

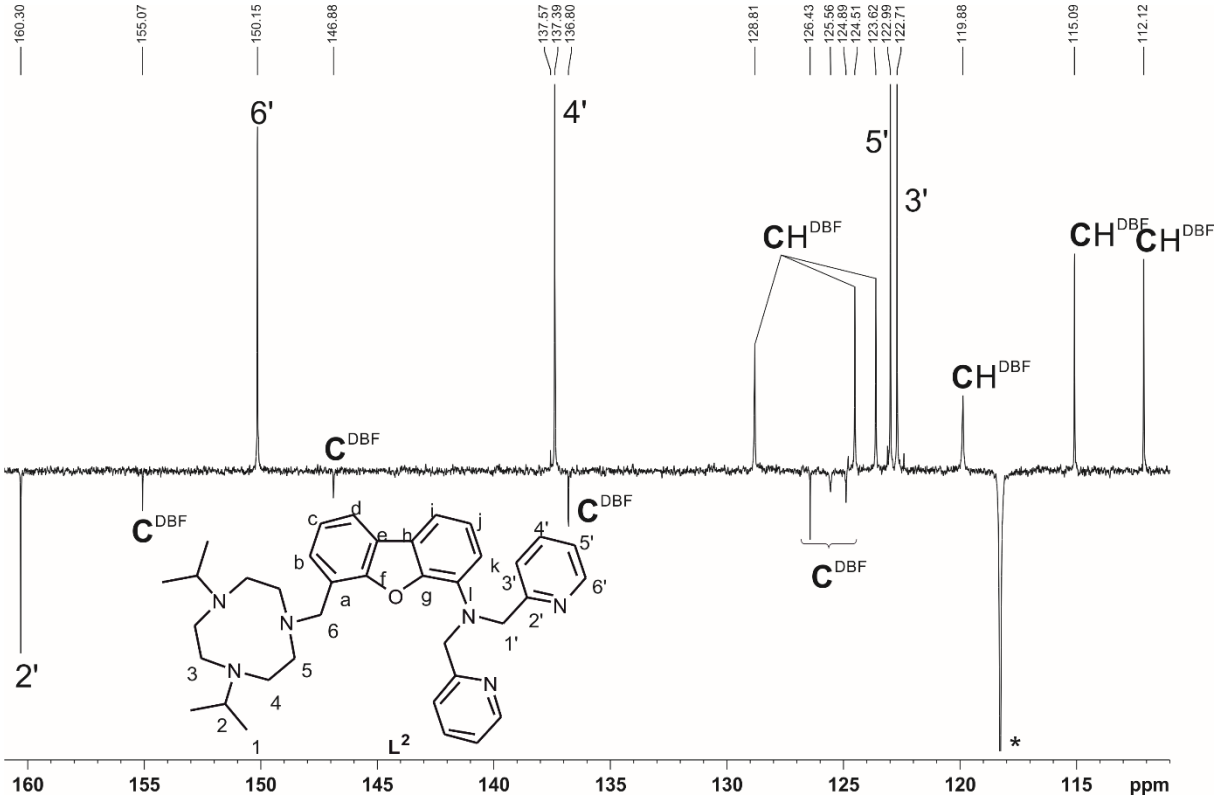

Figure S9. Magnified section of the ^{13}C APT NMR (100.6 MHz, 297 K) spectrum of $\mathbf{L^2}$ in CD_3CN showing the quaternary and aromatic C-atoms in the region 161-110 ppm. Quartenary and aromatic C-atoms of the dibenzofuran backbone that could not been clearly assigned were marked as $\mathbf{C}^{DBF}$ and $\mathbf{C}H^{DBF}$.

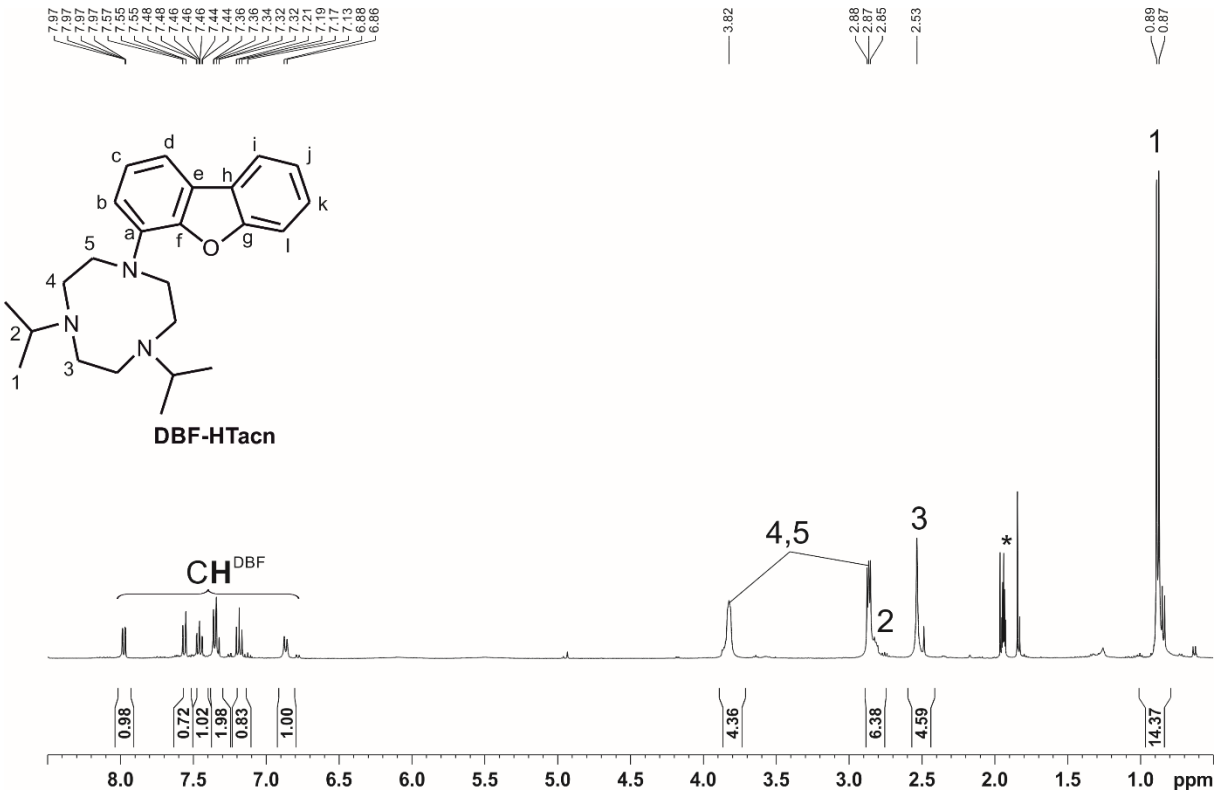

Figure S10. ^{1}H NMR (400.1 MHz, 297 K) spectrum of **DBF-HTacn** in CD_3CN.

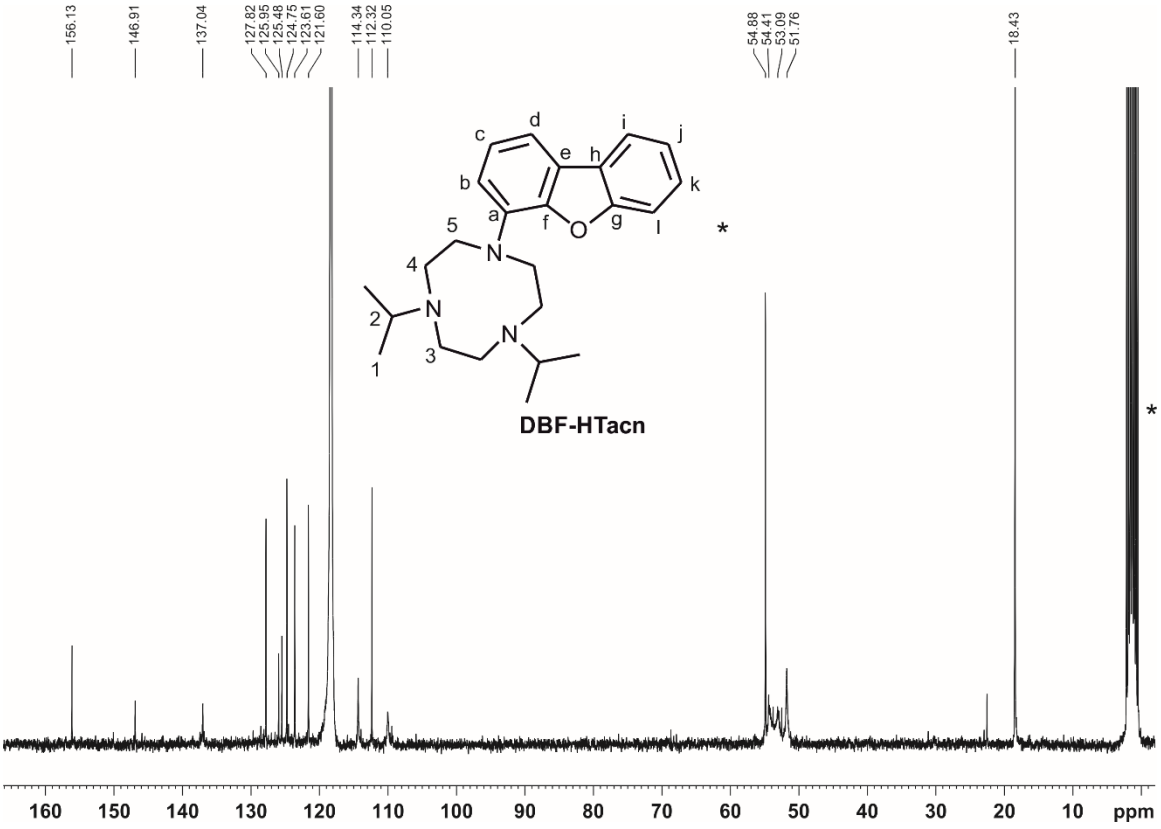

Figure S11. ^{13}C NMR (75.5 MHz, 297 K) apectrum of **DBF-HTacn** in CD_3CN.

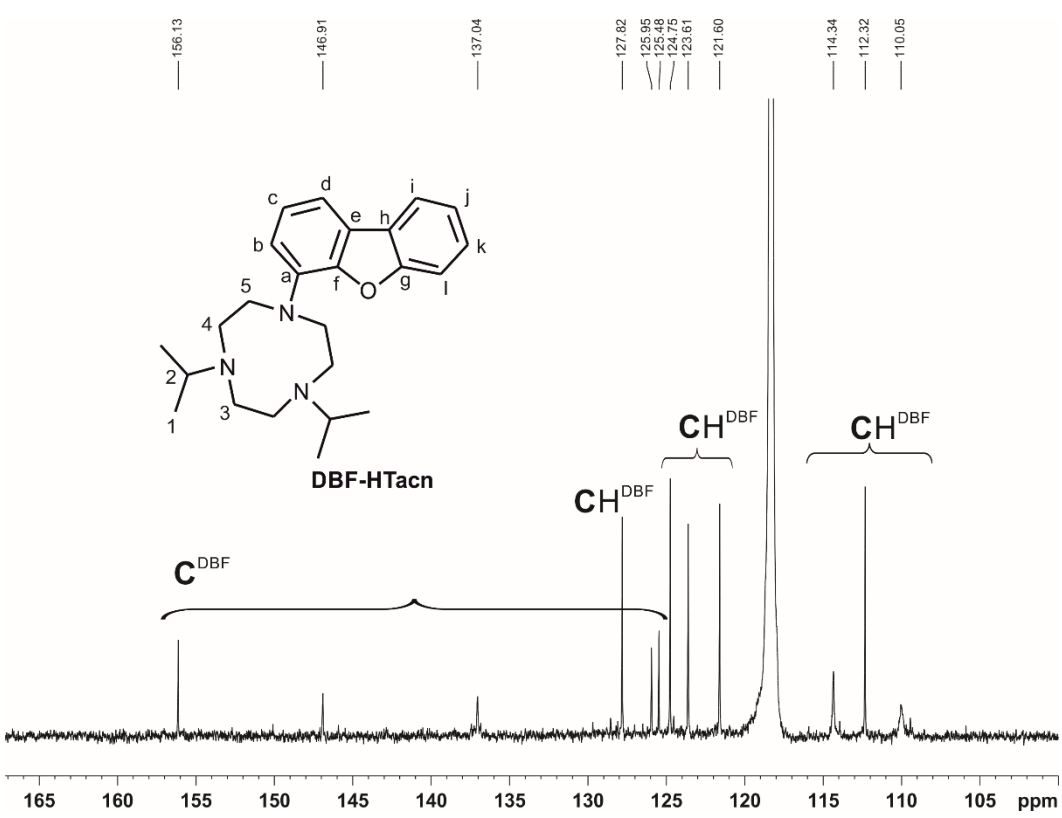

Figure S12. Magnified section of the ^{13}C NMR (75.5 MHz, 297 K) spectrum of **DBF-Tacn** in CD_3CN showing the quaternary and aromatic C-atoms in the region 165-100 ppm. Quartenary and aromatic C-atoms of the dibenzofuran backbone that could not been clearly assigned were marked as $\mathbf{C}^{DBF}$ and $\mathbf{C}H^{DBF}$.

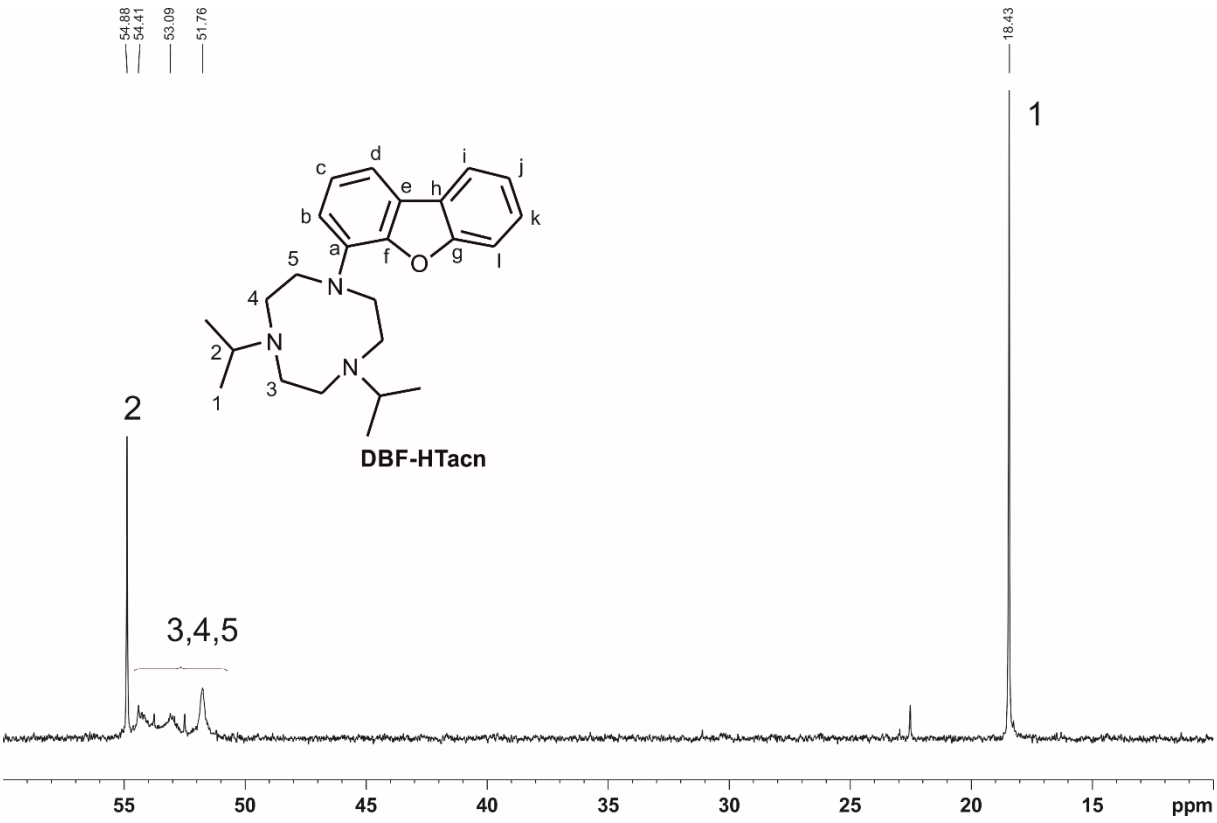

Figure S13. Magnified section of the ^{13}C NMR (100.6 MHz, 297 K) spectrum of **DBF-HTacn** in CD_3CN in the region 60-10 ppm.

Complexes

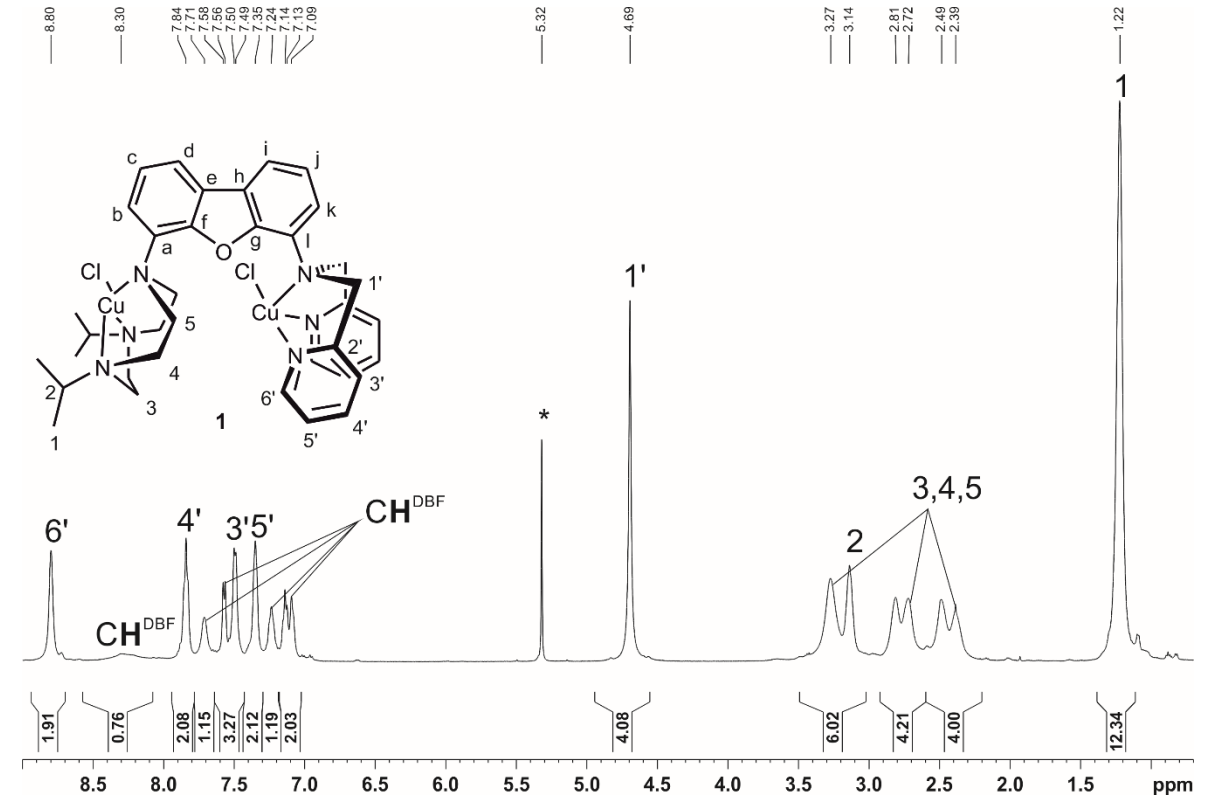

Figure S14. ^1H NMR (500.1 MHz, 297 K) spectrum of **1** in CD_2Cl_2.

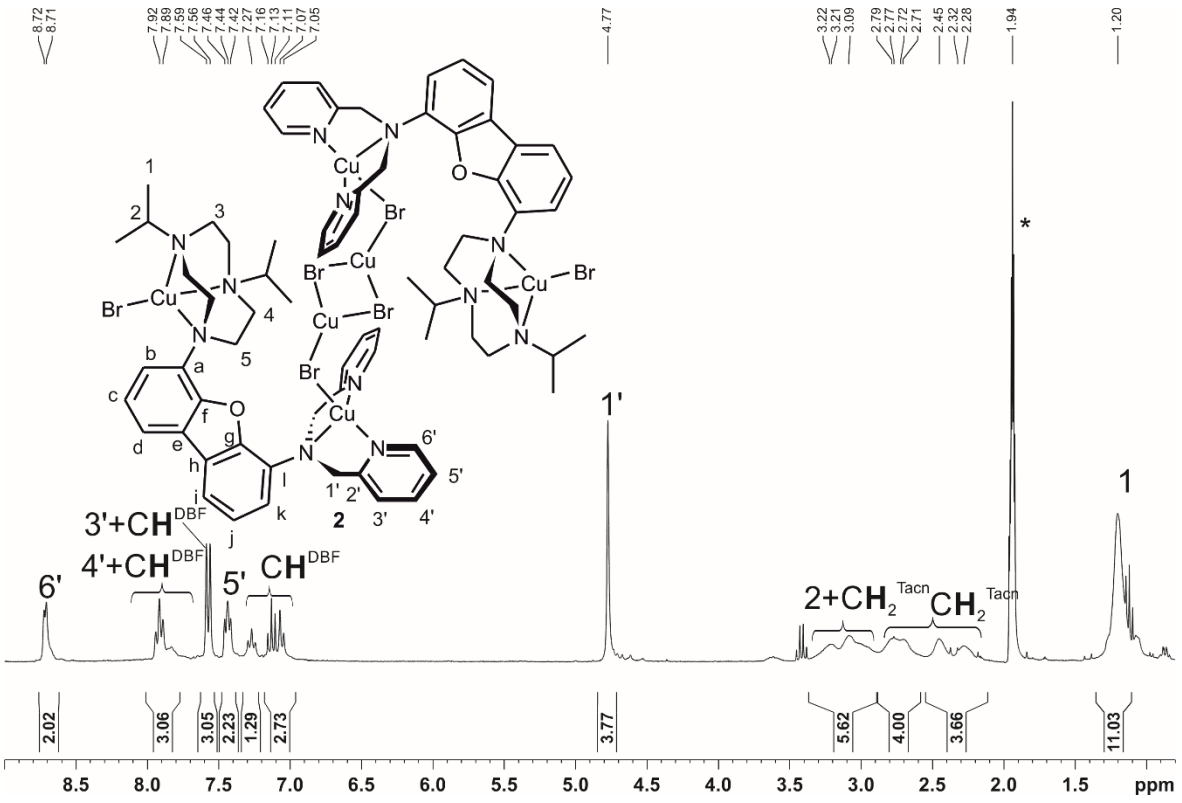

Figure S15. ^{1}H NMR (300.1 MHz, 297 K) spectrum of **2** in CD_3CN.

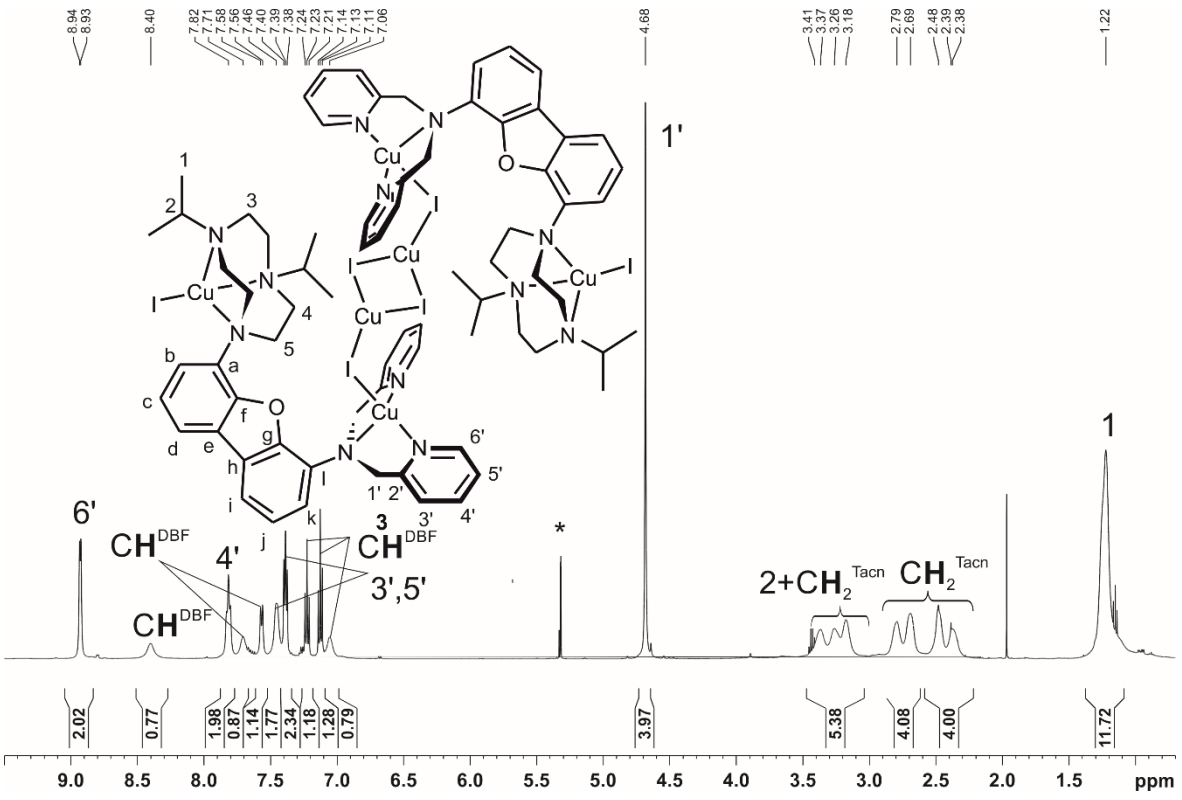

Figure S16. ^{1}H NMR (300.1 MHz, 297 K) spectrum of **3** in CD_2Cl_2.

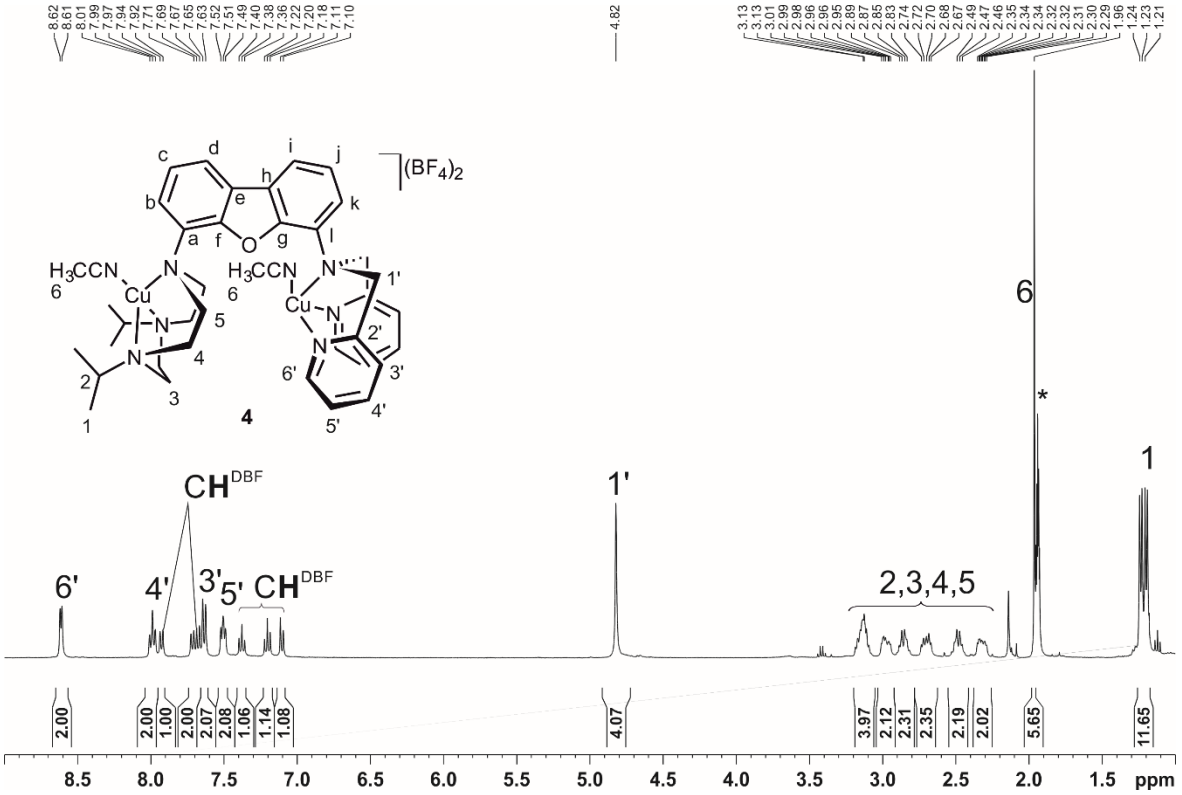

Figure S17. ^{1}H NMR (400.1 MHz, 297 K) spectrum of **4** in CD_3CN.

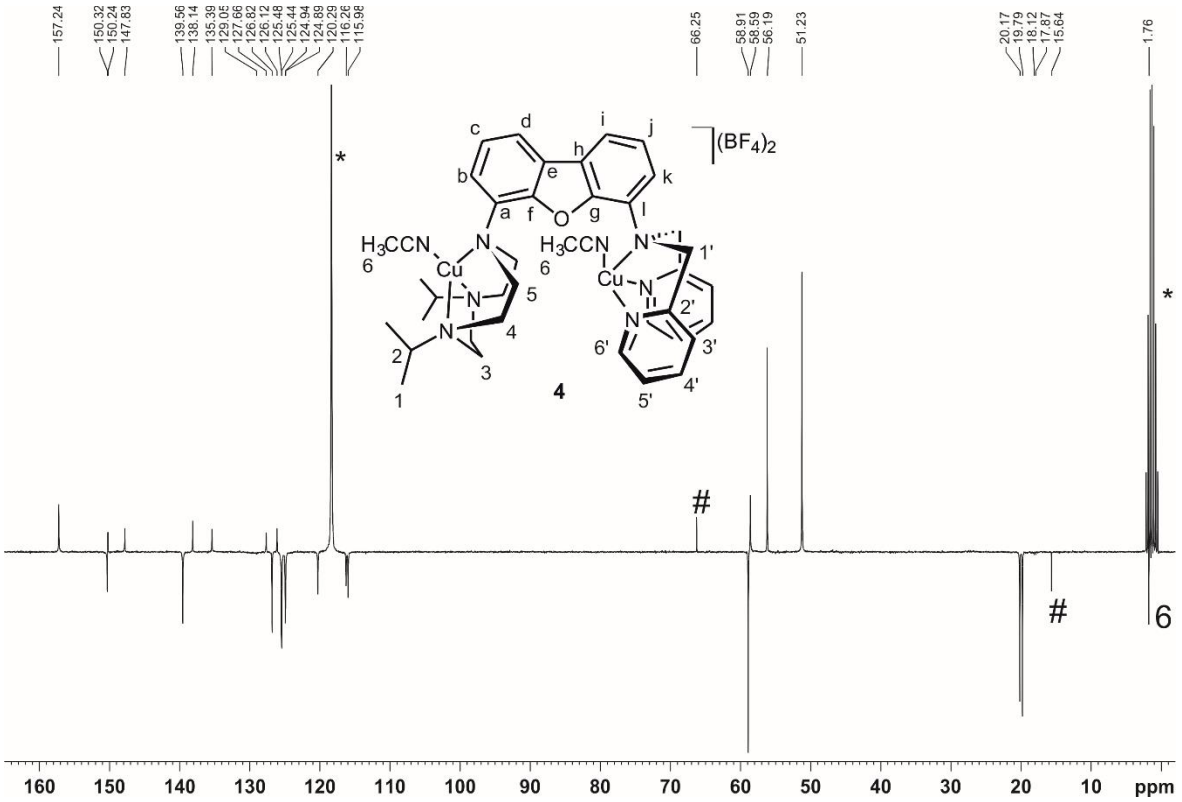

Figure S18. ^{13}C APT NMR (75.5 MHz, 297 K) spectrum of **4** in CD_3CN.

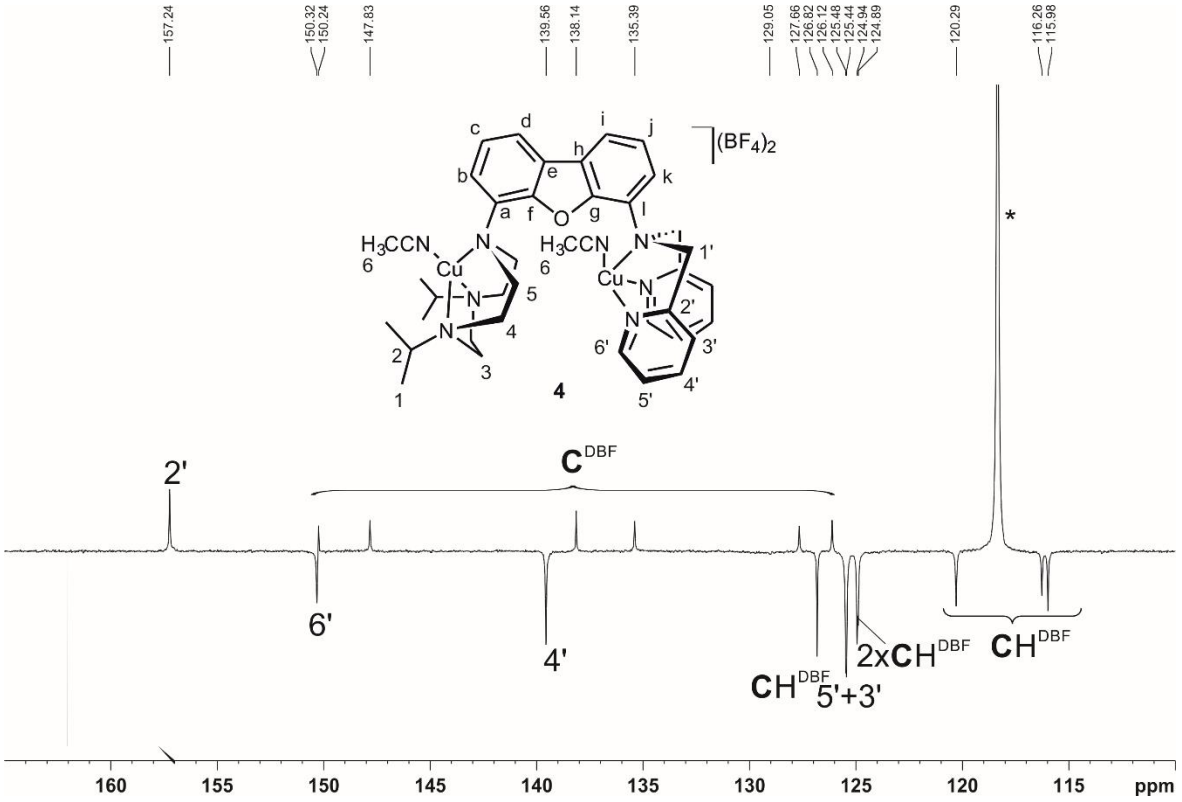

Figure S19. Magnified section of the ^{13}C APT NMR (75.5 MHz, 297 K) spectrum of **4** in CD_3CN showing the quaternary and aromatic C-atoms in the region 170-110 ppm. Quartenary and aromatic C-atoms of the dibenzofuran backbone that could not been clearly assigned were marked as $\mathbf{C}^{DBF}$ and $\mathbf{C}H^{DBF}$.

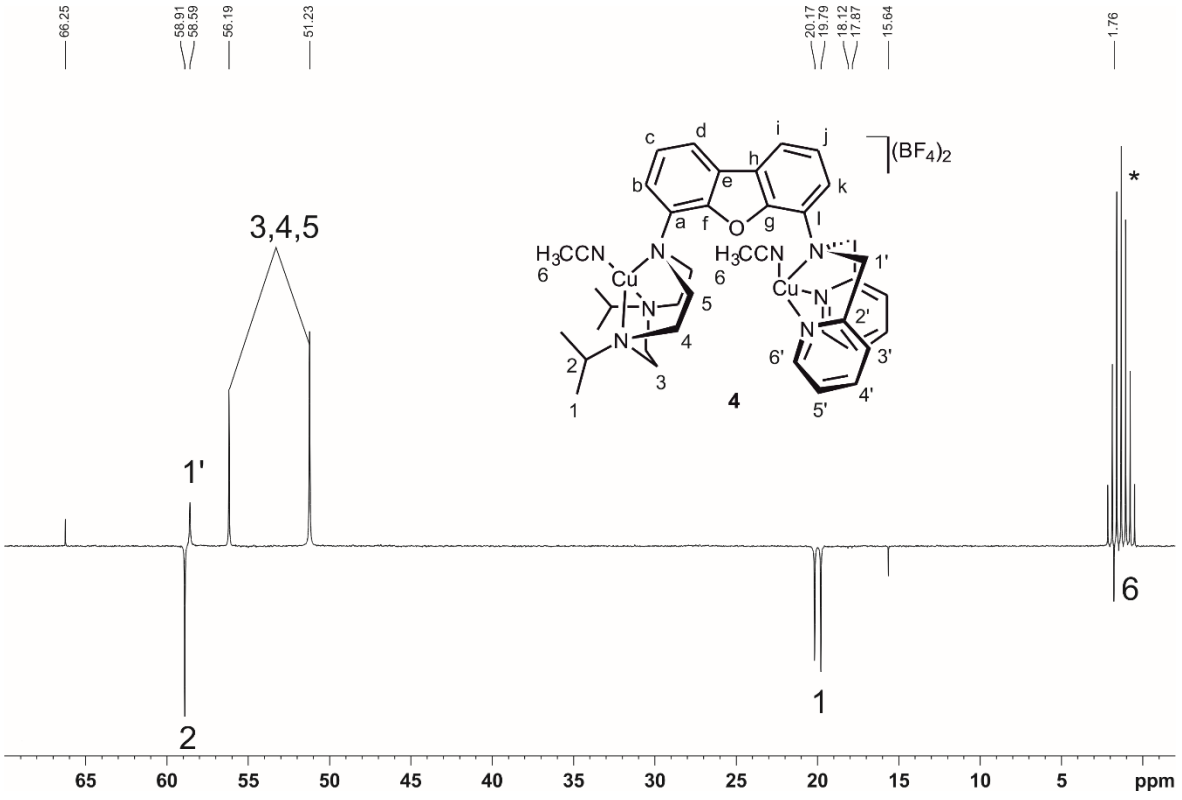

Figure S20. Magnified section of the ^{13}C APT NMR (100.6 MHz, 297 K) spectrum of **4** in CD_3CN in the region 70-0 ppm.

Since the ^{1}H and $^{13}C/^{13}C$ APT NMR spectra of the complexes **4**-**6** are very similar, no assignment of the signals were made for the complexes **5** and **6**.

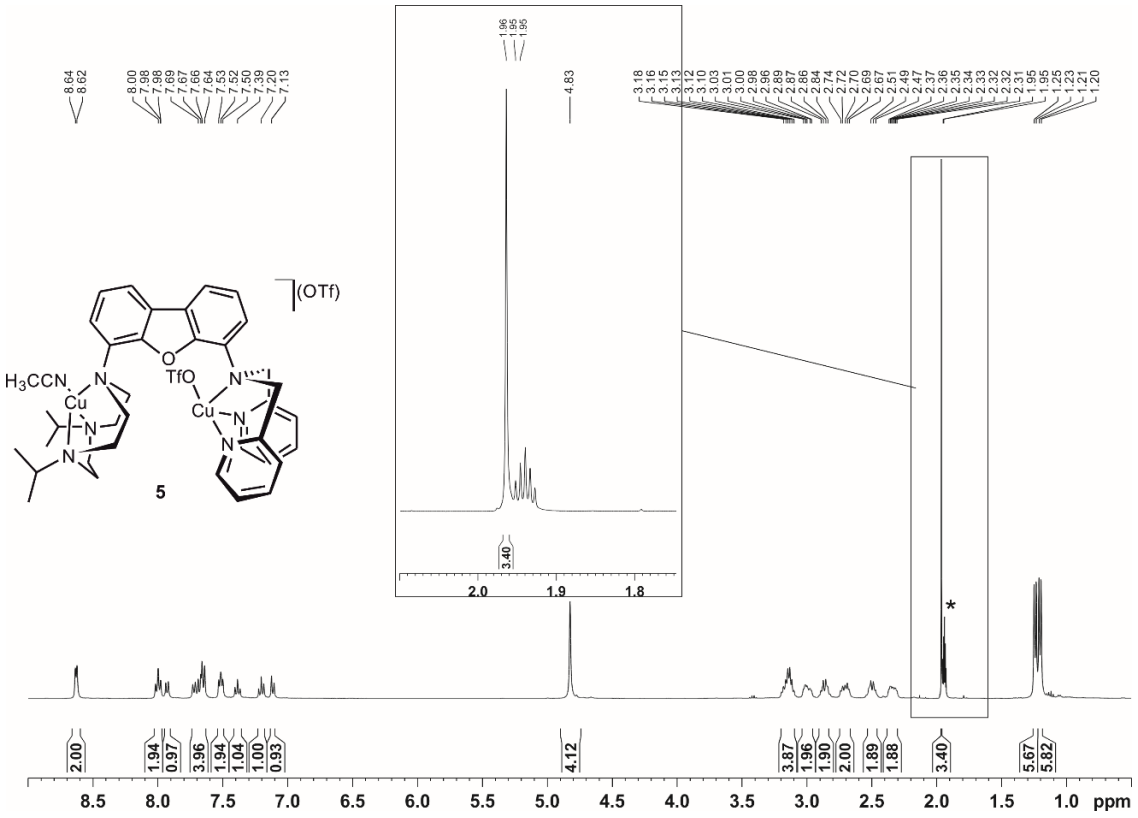

Figure S21. ^{1}H NMR (400.1 MHz, 297 K) spectrum of **5** in CD_3CN.

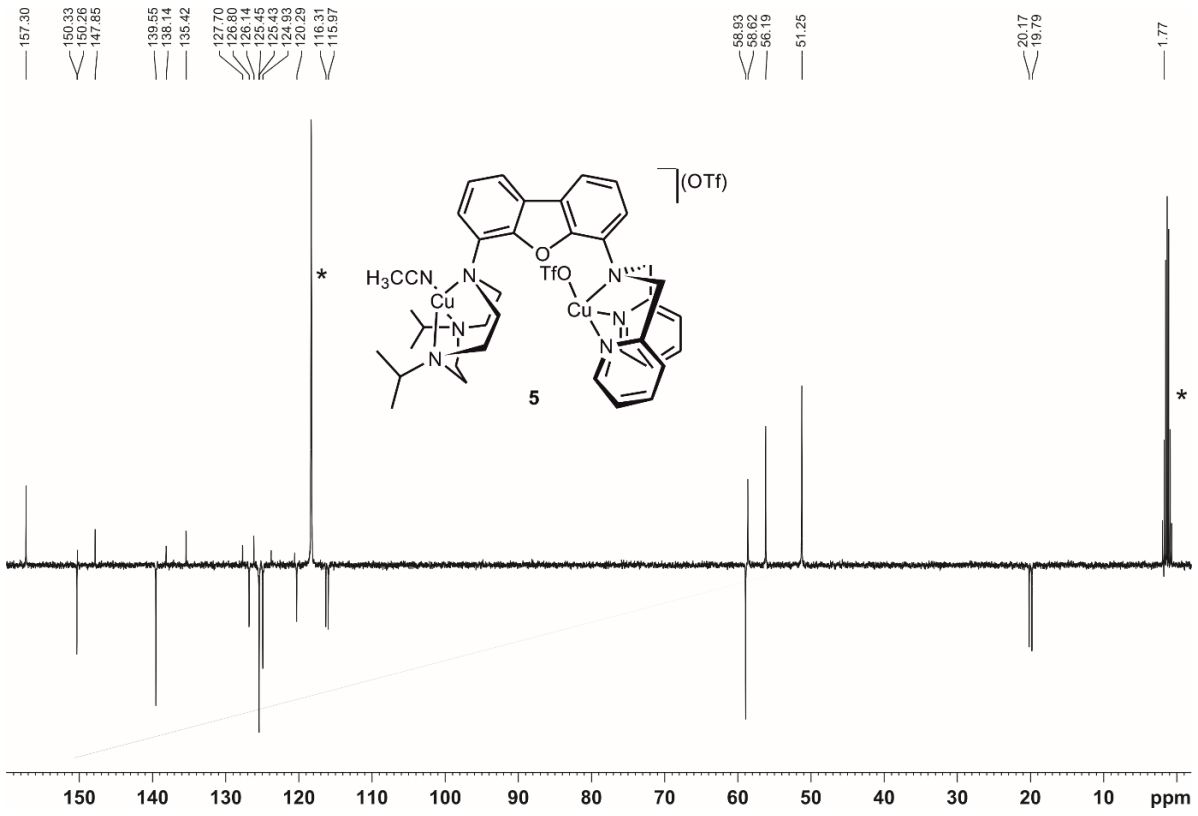

Figure S22. ^{13}C APT NMR (100.6 MHz, 297 K) spectrum of **5** in CD_3CN.

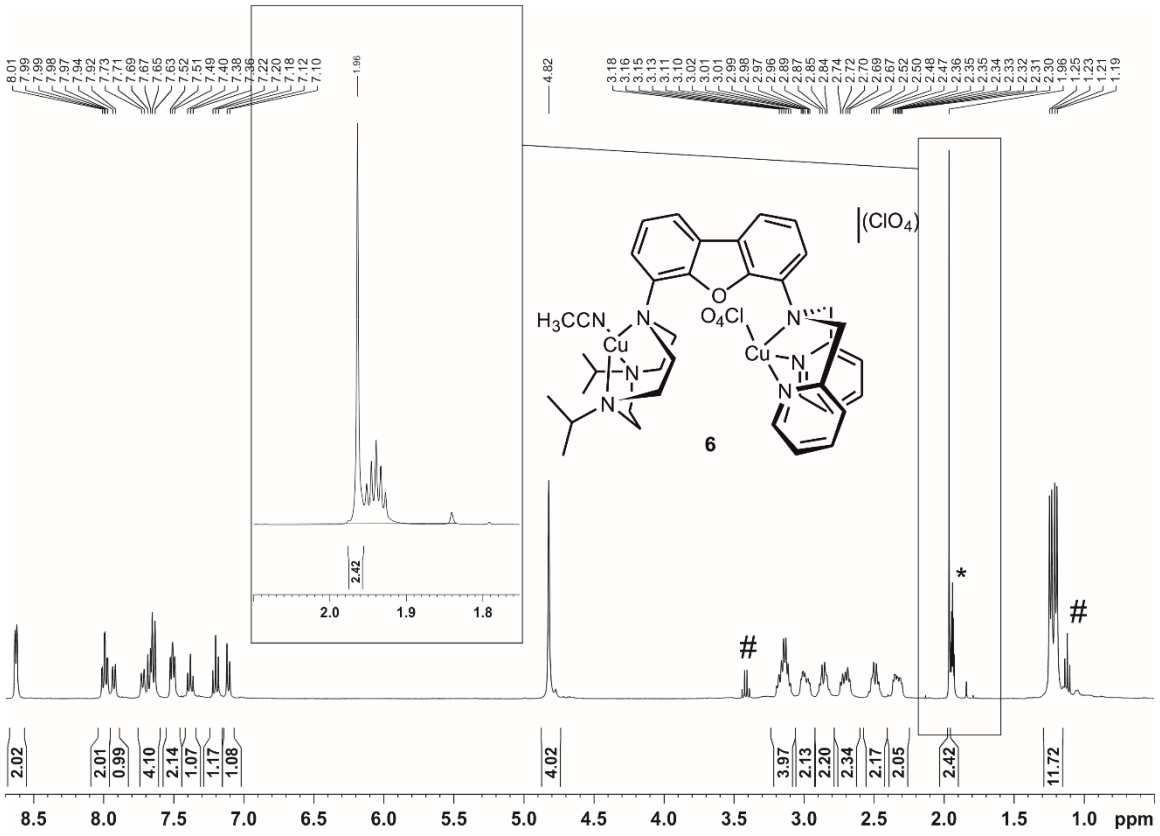

Figure S23. ^{1}H NMR (400.1 MHz, 297 K) spectrum of **6** in CD_3CN.

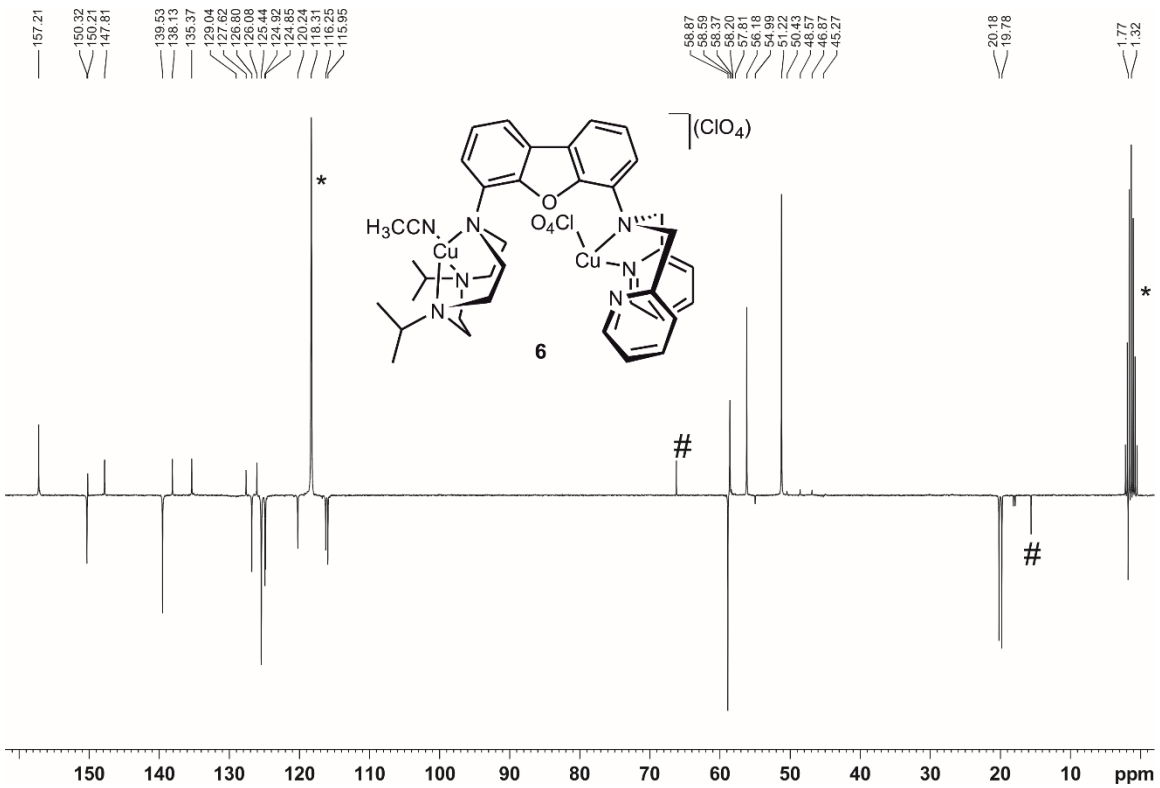

Figure S24. ^{13}C APT NMR (75.5 MHz, 297 K) spectrum of **6** in CD_3CN.

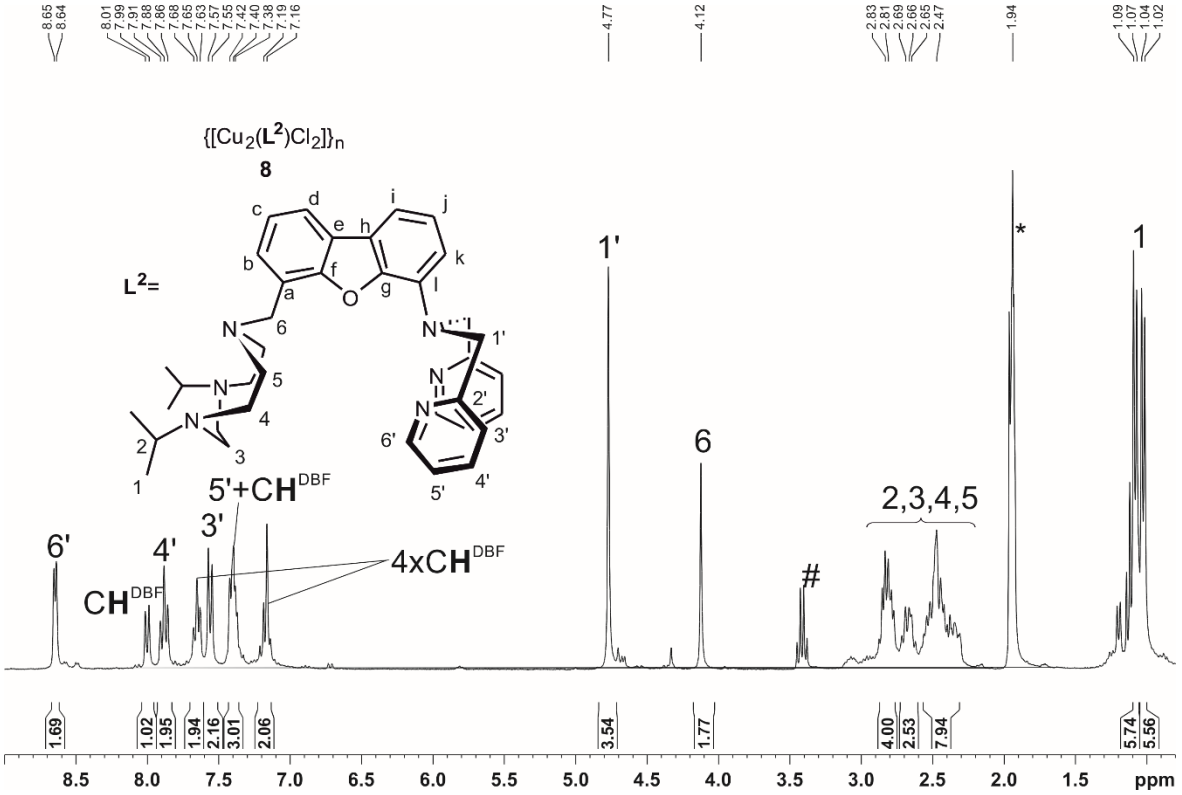

Figure S25. ^{1}H NMR (300.1 MHz, 297 K) spectrum of **8** in CD_3CN.

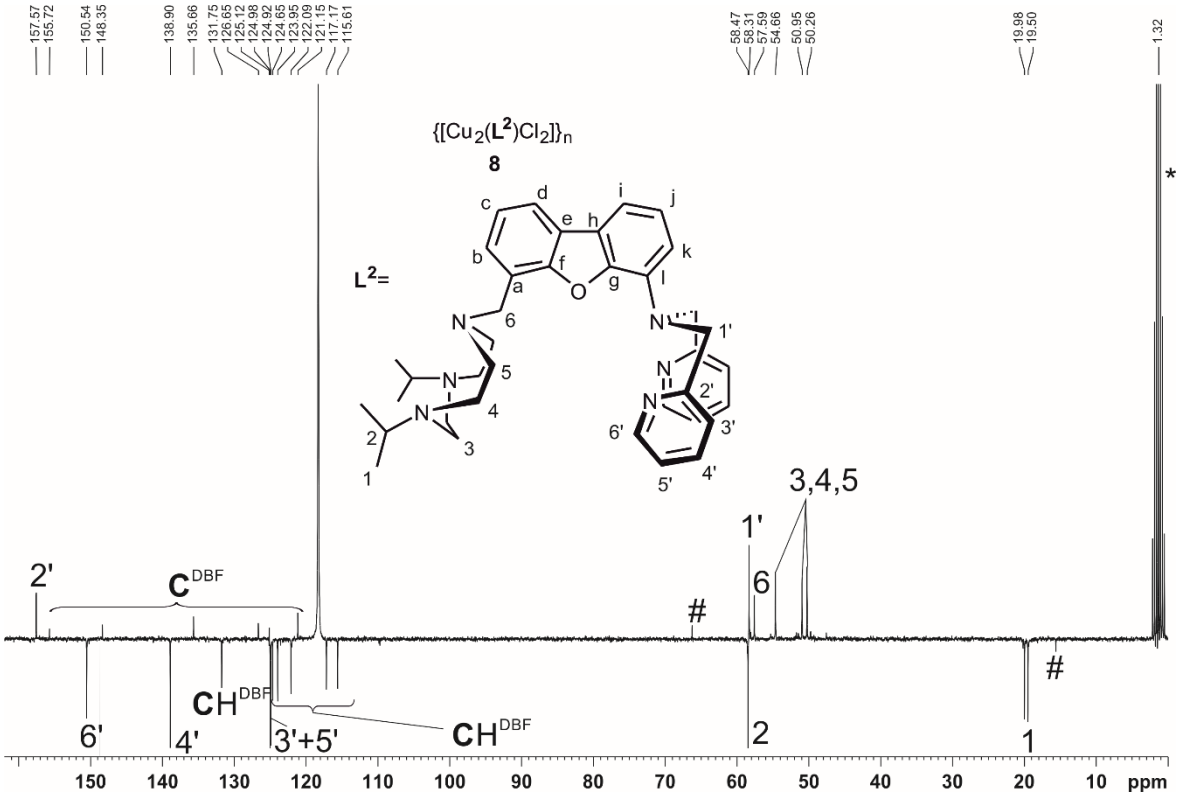

Figure S26. ^{13}C APT NMR (75.5 MHz, 297 K) spectrum of **8** in CD_3CN.

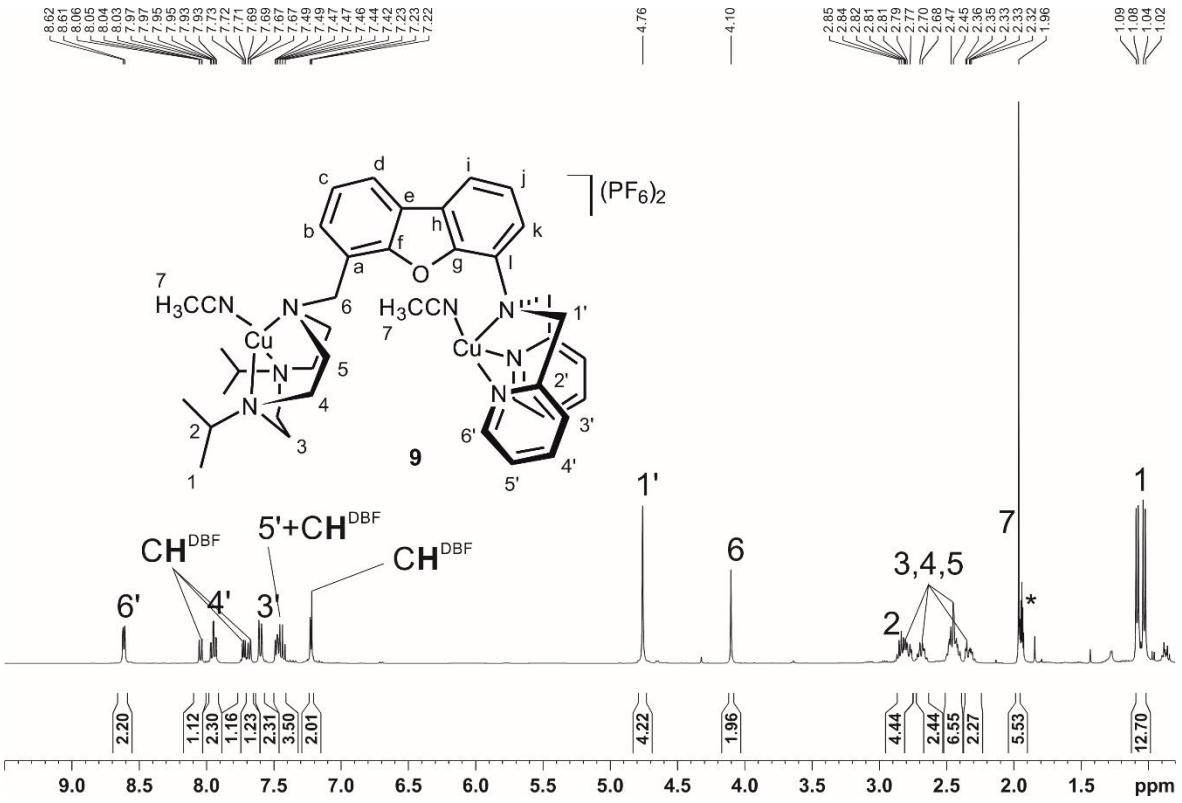

Figure S27. ^{1}H NMR (400.1 MHz, 297 K) spectrum of **9** in CD_3CN.

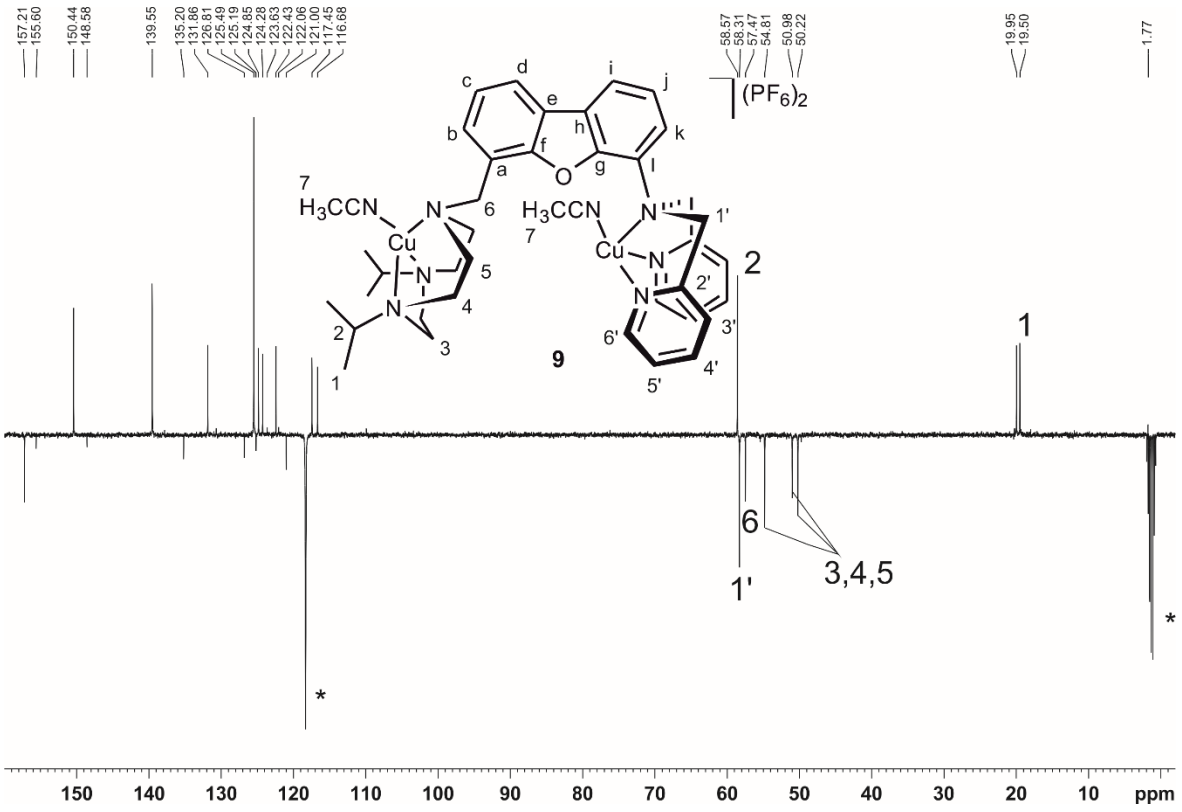

Figure S28. ^{13}C APT NMR (100.6 MHz, 297 K) spectrum of **9** in CD_3CN.

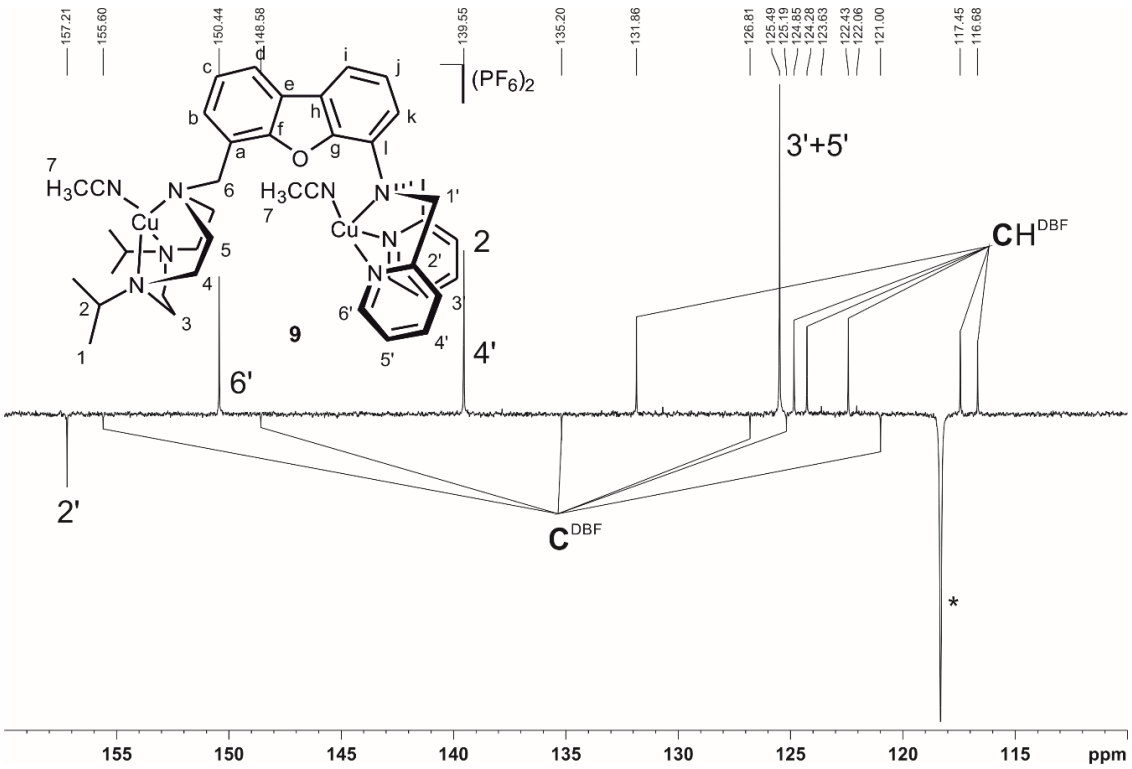

Figure S29. Magnified section of the ^{13}C APT NMR (100.6 MHz, 297 K) spectrum of **9** in CD_3CN showing the quaternary and aromatic C-atoms in the region 160-110 ppm. Quartenary and aromatic C-atoms of the dibenzofuran backbone that could not been clearly assigned were marked as $\mathbf{C}^{DBF}$ and $\mathbf{CH}^{DBF}$.

Since the ^{1}H and $^{13}C/^{13}C$ APT NMR spectra of the complexes **9** and **10** are very similar, no assignment of the signals were made for complex **10**.

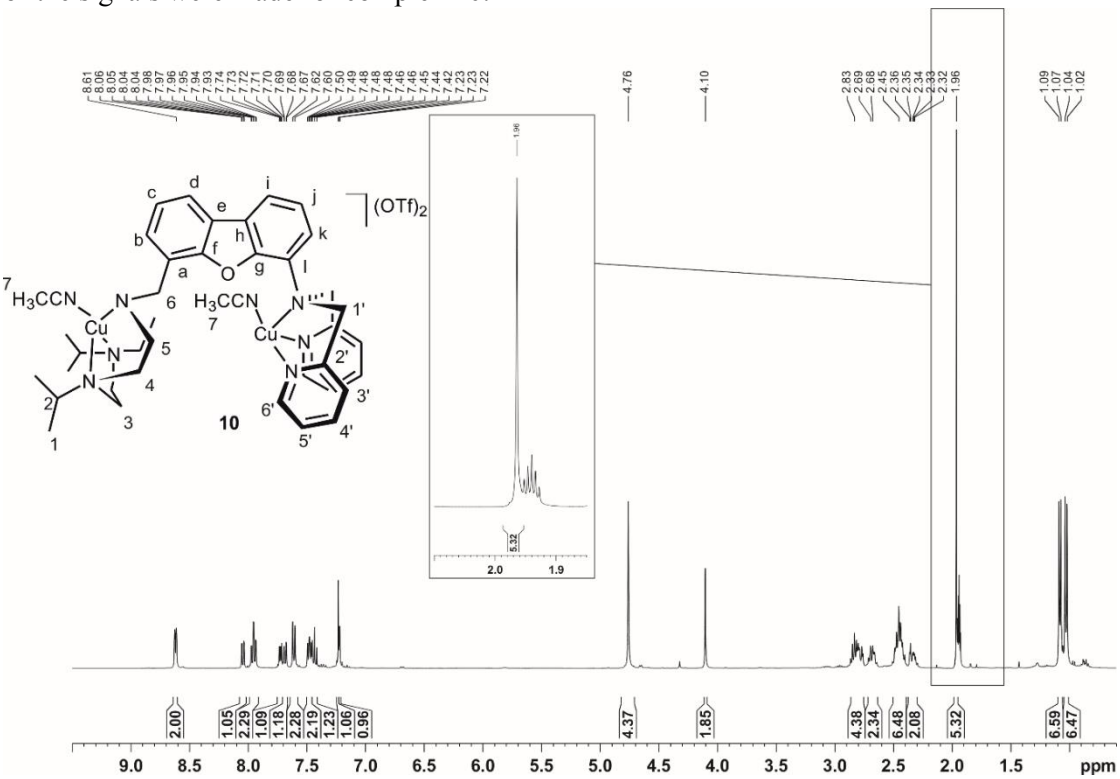

Figure S30. ^{1}H NMR (400.1 MHz, 297 K) spectrum of **10** in CD_3CN.

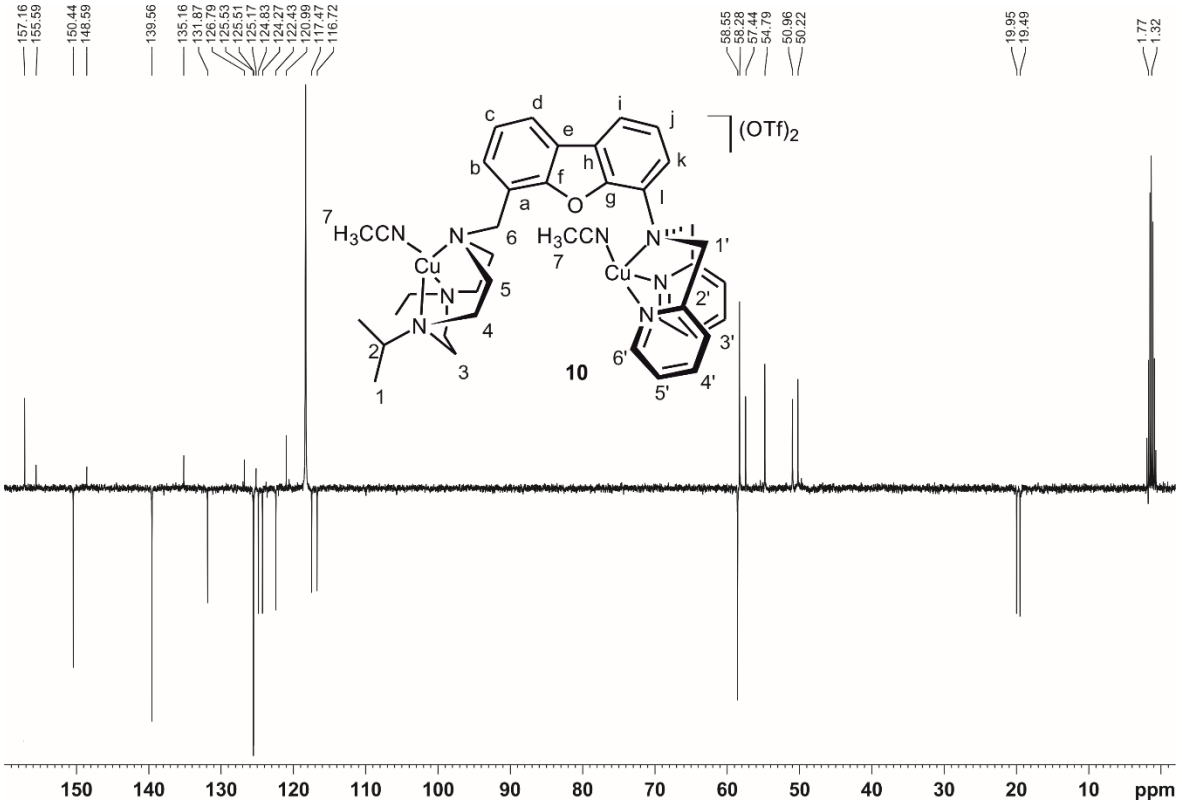

Figure S31. ^{13}C APT NMR (100.6 MHz, 297 K) spectrum of **10** in CD_3CN.

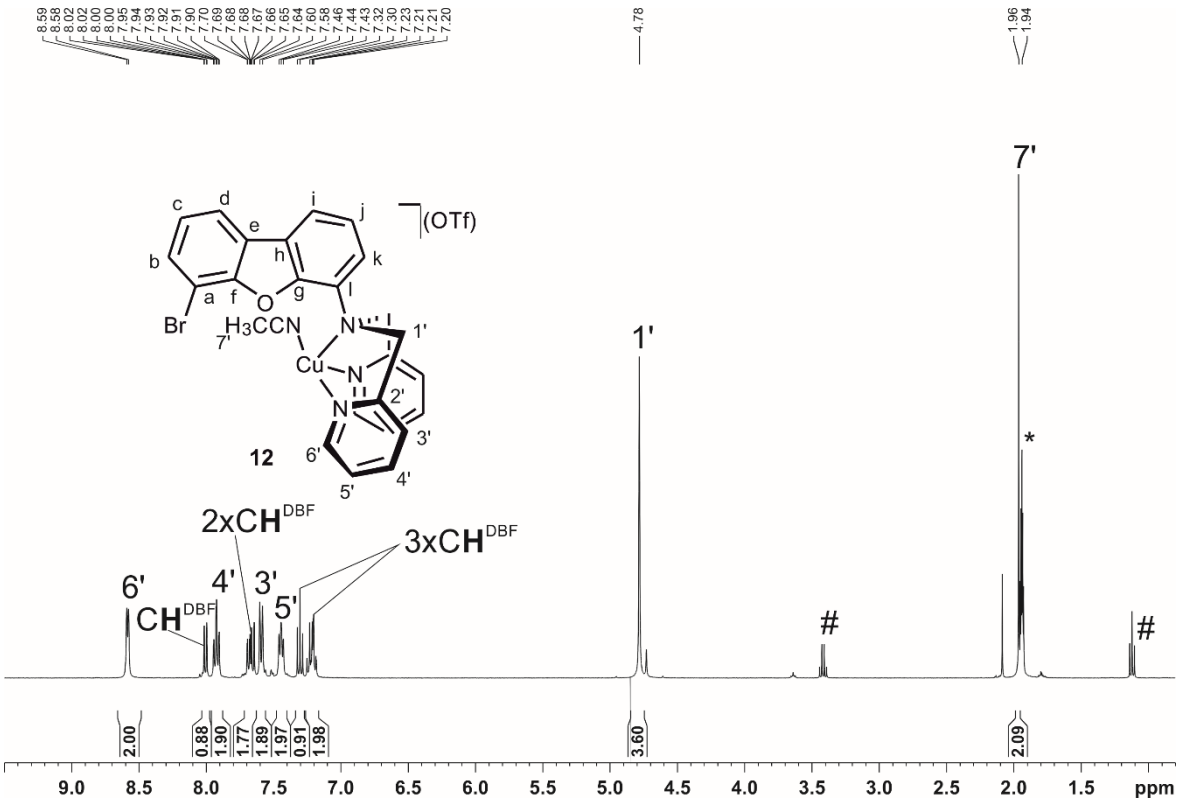

Figure S32. ^{1}H NMR (400.1 MHz, 297 K) spectrum of **12** in CD_3CN.

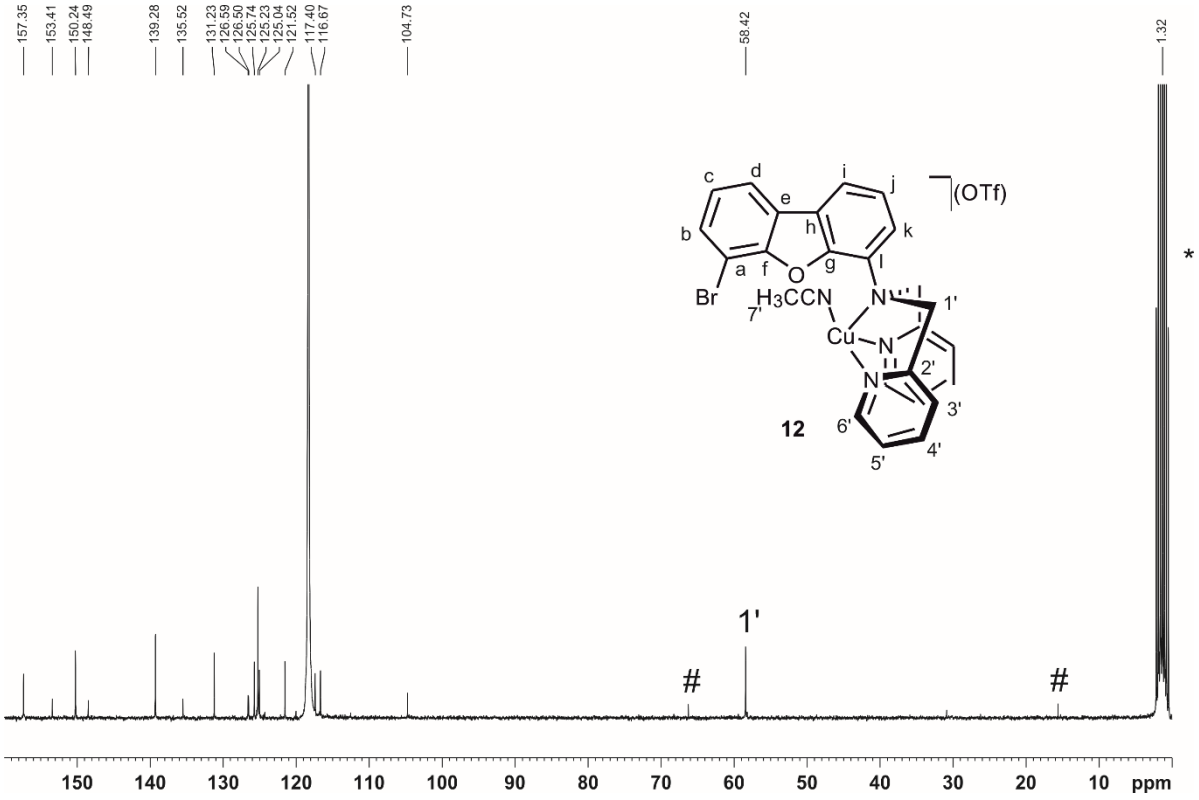

Figure S33. ^{13}C NMR (75.5 MHz, 297 K) spectrum of **12** in CD_3CN.

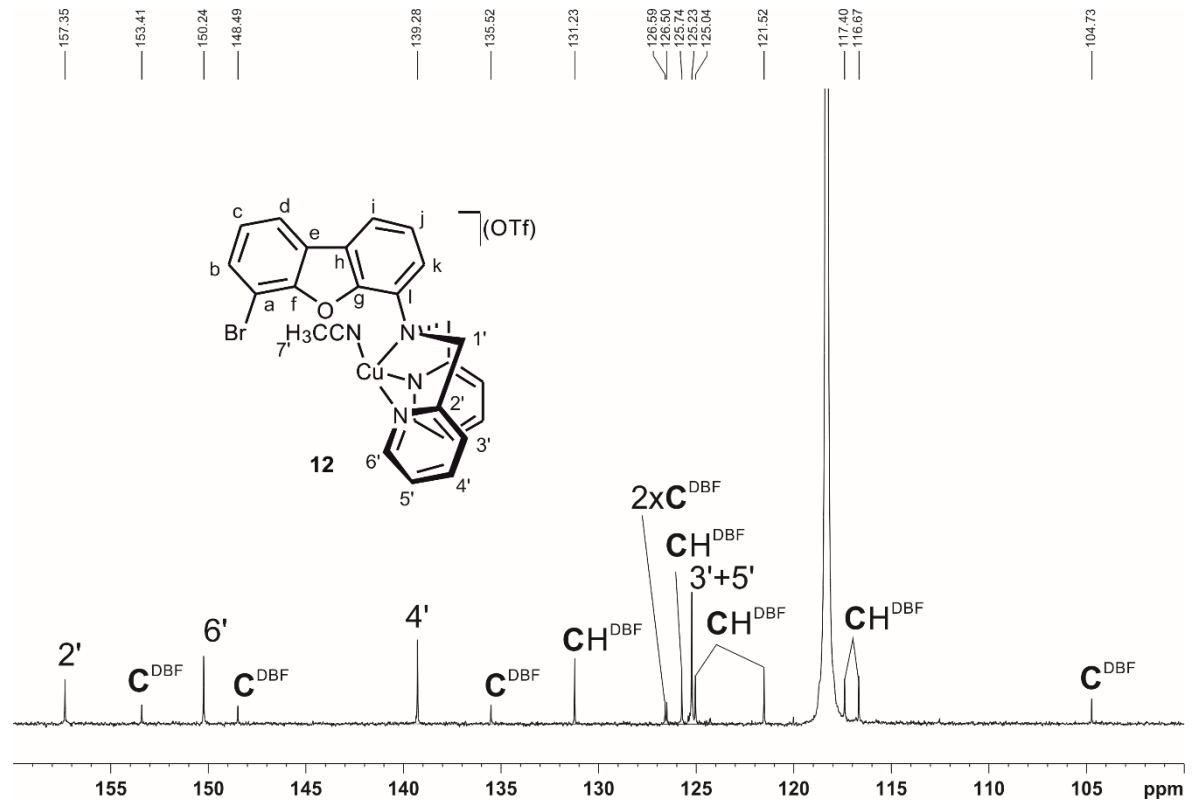

Figure S34. Magnified section of the ^{13}C APT NMR (100.6 MHz, 297 K) spectrum of **12** in CD_3CN showing the quaternary and aromatic C-atoms in the region 160-100 ppm. Quartenary and aromatic C-atoms of the dibenzofuran backbone that could not been clearly assigned were marked as $\mathbf{C}^{DBF}$ and $\mathbf{C}H^{DBF}$.

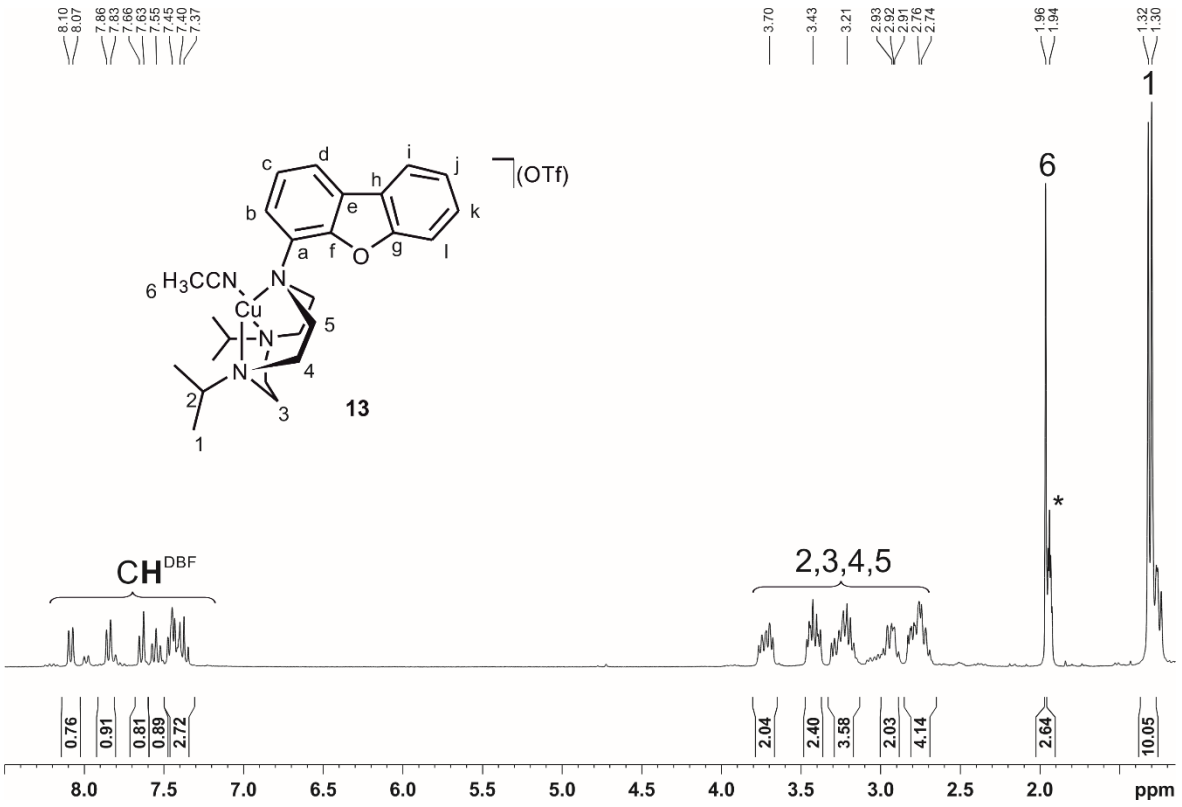

Figure S35. ^{1}H NMR (400.1 MHz, 297 K) spectrum of **13** in CD_3CN.

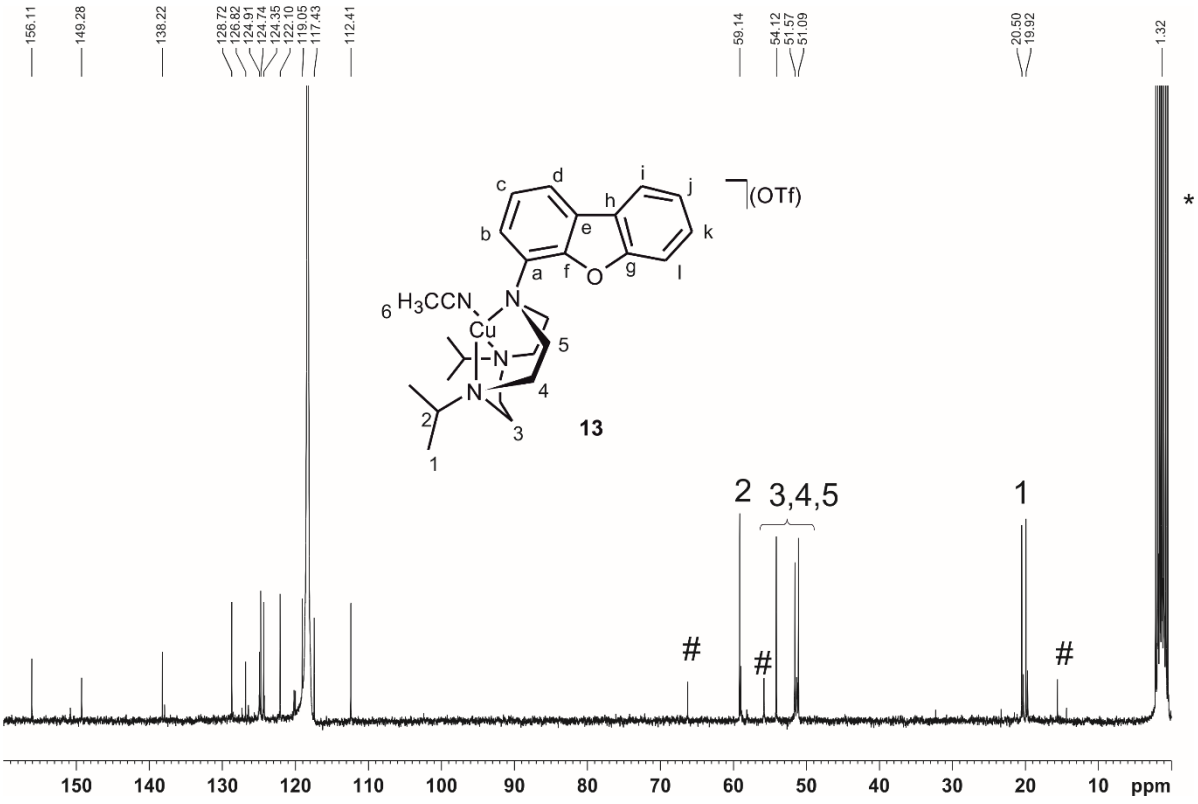

Figure S36. ^{13}C NMR (75.5 MHz, 297 K) spectrum of **13** in CD_3CN.

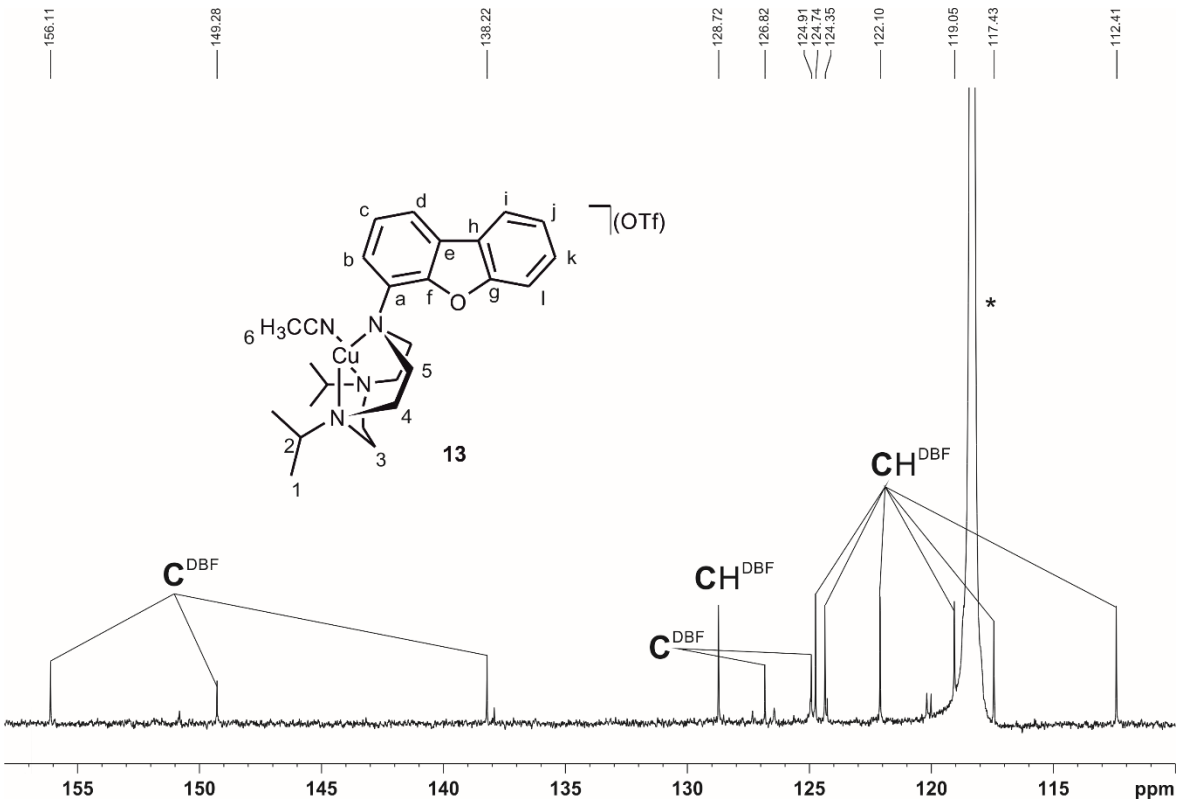

Figure S37. Magnified section of the ^{13}C APT NMR (100.6 MHz, 297 K) spectrum of **12** in CD_3CN showing the quaternary and aromatic C-atoms in the region 160-100 ppm. Quartenary and aromatic C-atoms of the dibenzofuran backbone that could not been clearly assigned were marked as $\mathbf{C}^{DBF}$ and $\mathbf{C}H^{DBF}$.

3. Mass spectra

Ligands

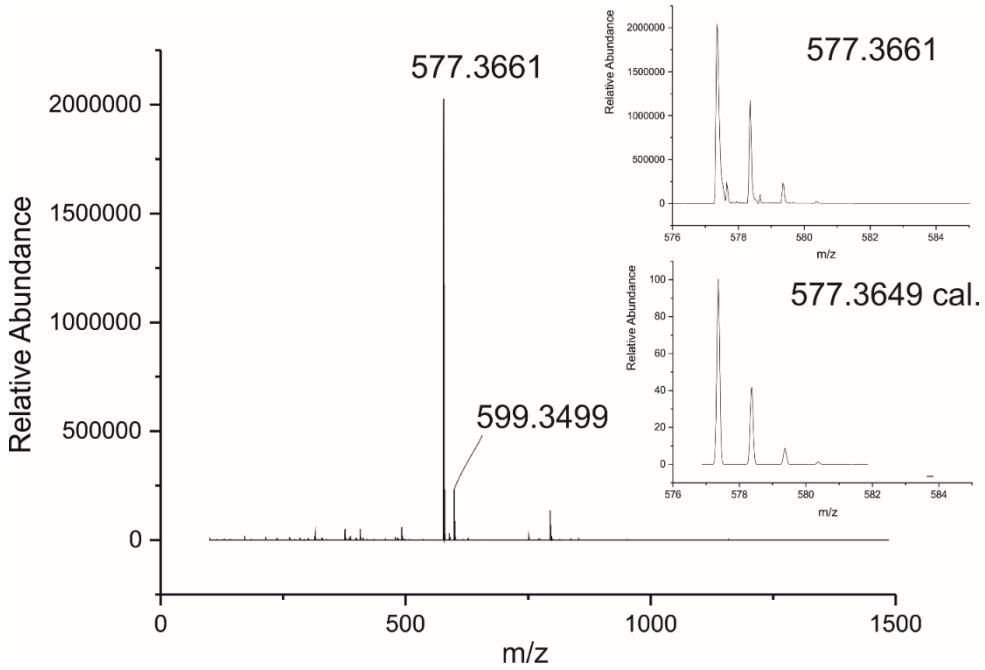

Figure S38. ESI-MS of $\mathbf{L^1}$ in acetonitrile. The inserted graphs show the measured (top) and calculated (below) isotopic pattern for the peak at m/z = 577.3661 corresponding to $[(\mathbf{L^1})+H]^+$.

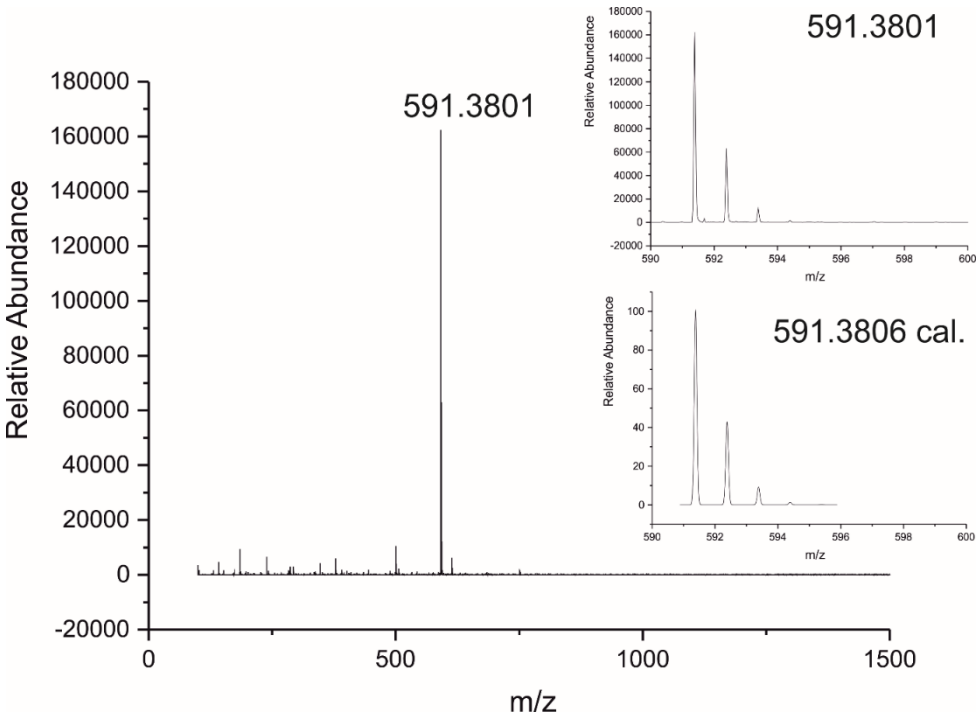

Figure S39. ESI-MS of $\mathbf{L^2}$ in acetonitrile. The inserted graphs show the measured (top) and calculated (below) isotopic pattern for the peak at m/z = 591.3801 corresponding to $[(\mathbf{L^2})+H]^+$.

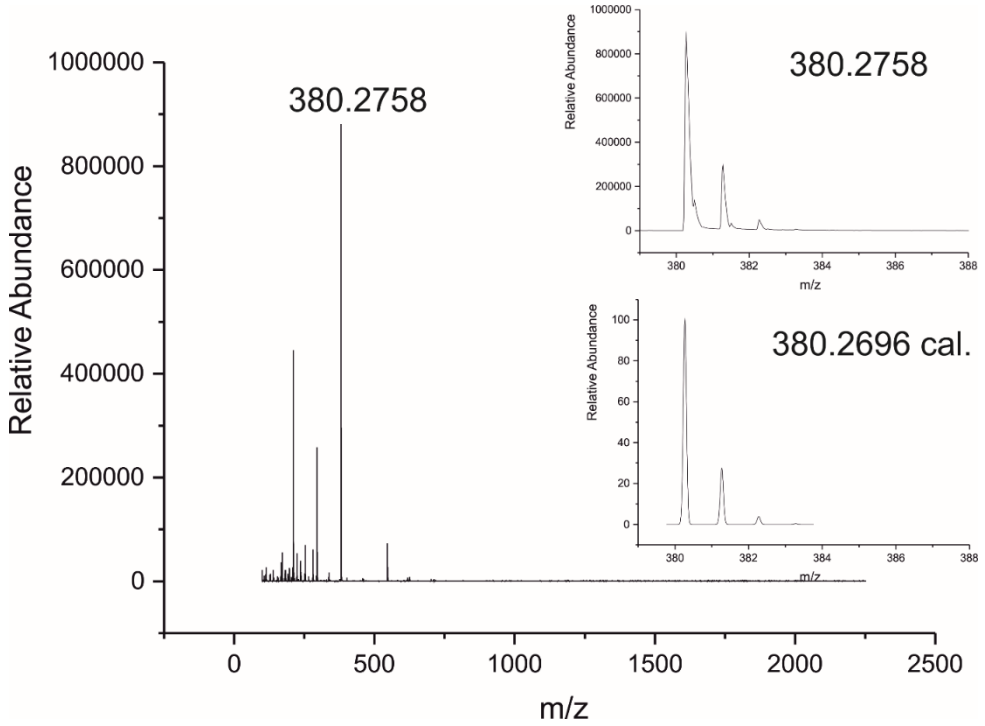

Figure S40. ESI-MS of **DBF-HTacn** in acetonitrile. The inserted graphs show the measured (top) and calculated (below) isotopic pattern for the peak at m/z = 380.2758 corresponding to [(**DBF-HTacn**)+H]$^+$.

Complexes

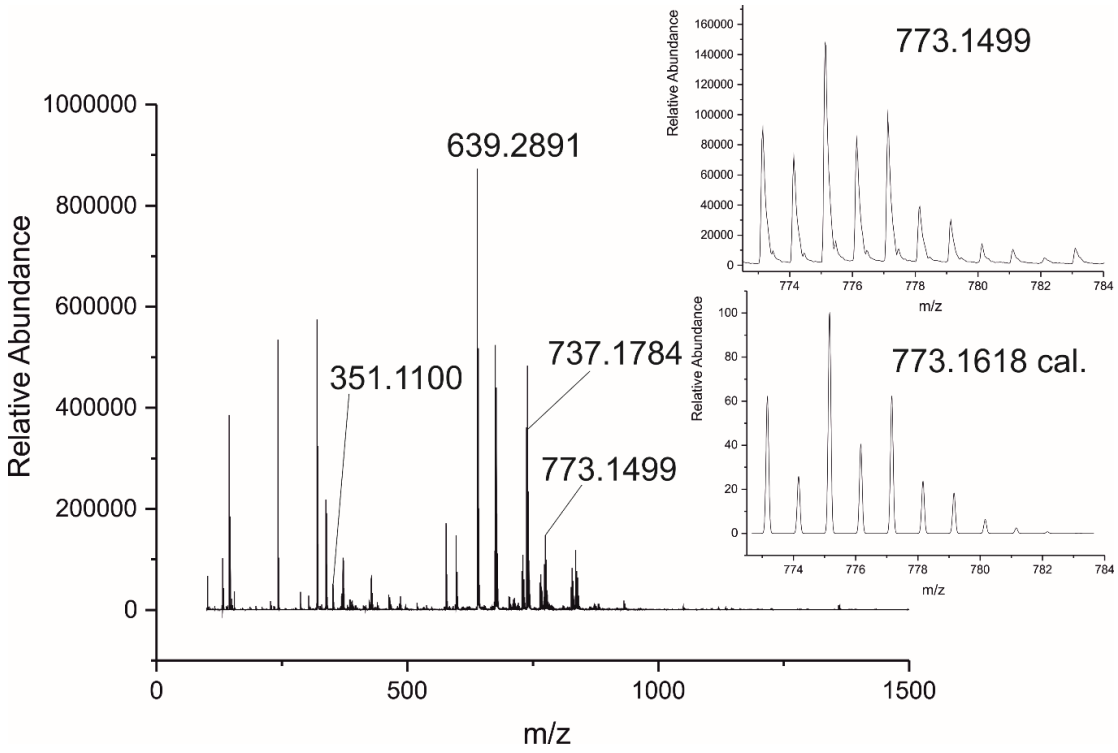

Figure S41. ESI-MS of **1** in acetonitrile. The inserted graphs show the measured (top) and calculated (below) isotopic pattern for the peak at m/z = 773.1499 corresponding to [(**L**^{1})$(CuCl)_2$+H]$^+$.

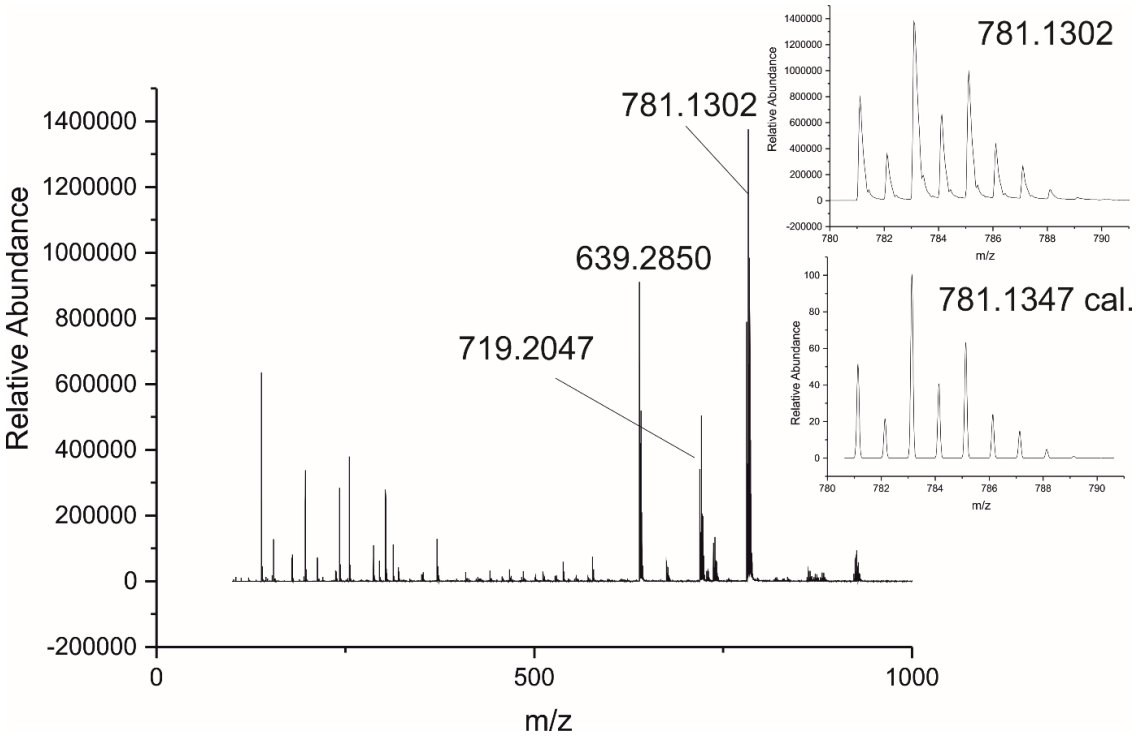

Figure S42. ESI-MS of **2** in acetone. The inserted graphs show the measured (top) and calculated (below) isotopic pattern for the peak at m/z = 781.1302 corresponding to $[(\mathbf{L^1})(Cu)_2Br]^+$.

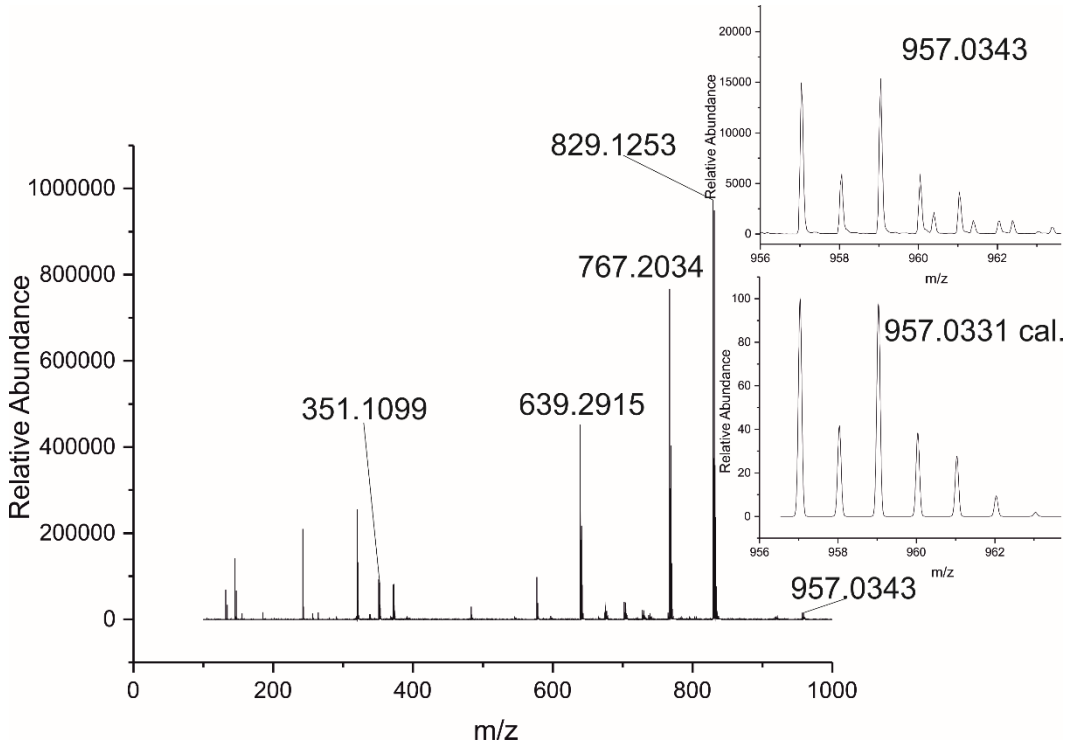

Figure S43. ESI-MS of **3** in acetonitrile. The inserted graphs show the measured (top) and calculated (below) isotopic pattern for the peak at m/z = 957.0343 corresponding to $[(\mathbf{L^1})(CuI)_2+H]^+$.

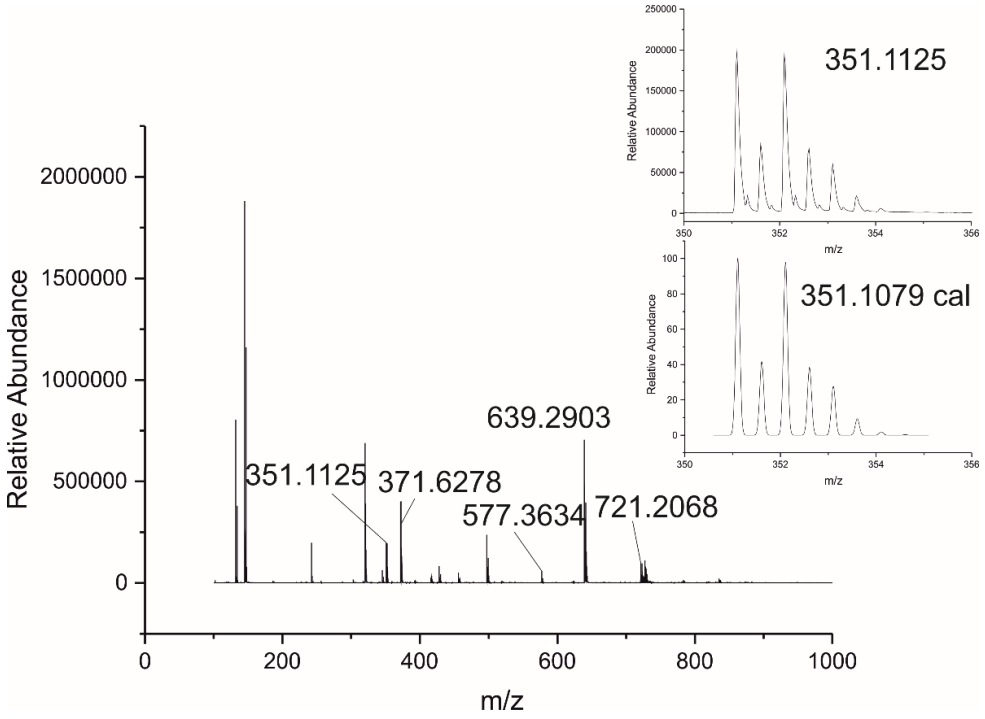

Figure S44. ESI-MS of **4** in acetonitrile. The inserted graphs show the measured (top) and calculated (below) isotopic pattern for the peak at m/z = 351.1125 corresponding to $[(\mathbf{L^1})(Cu)_2]^{2+}$.

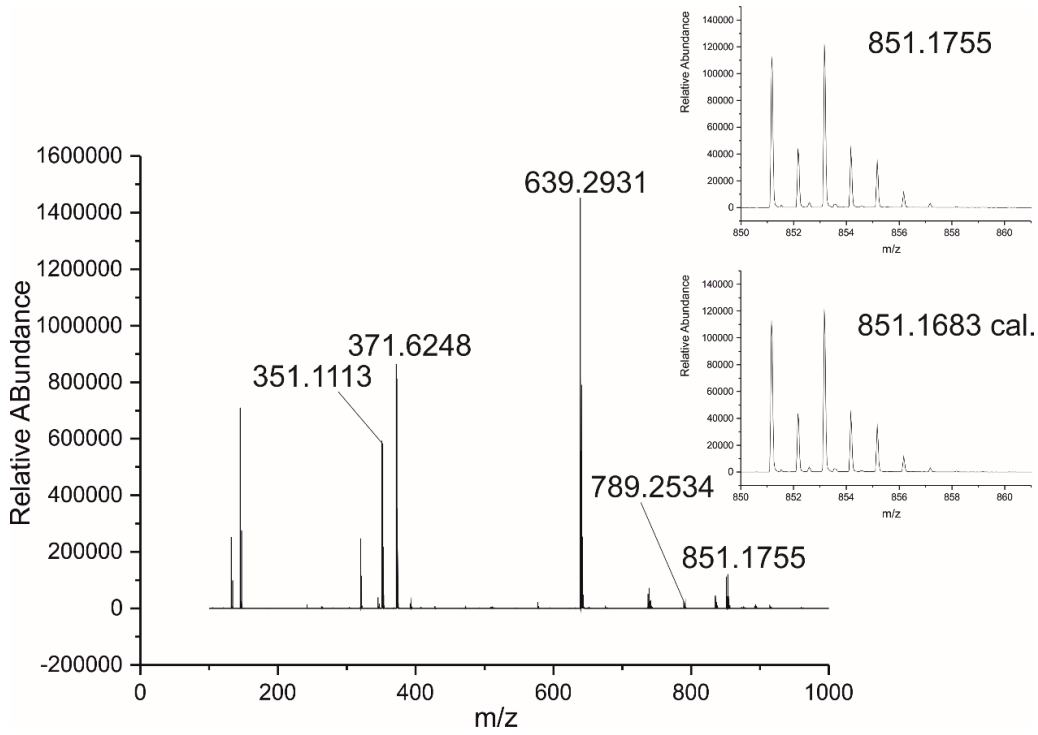

Figure S45. ESI-MS of **5** in acetonitrile. The inserted graphs show the measured (top) and calculated (below) isotopic pattern for the peak at m/z = 851.1755 corresponding to $[(\mathbf{L^1})(Cu)_2+OTf]^{+}$.

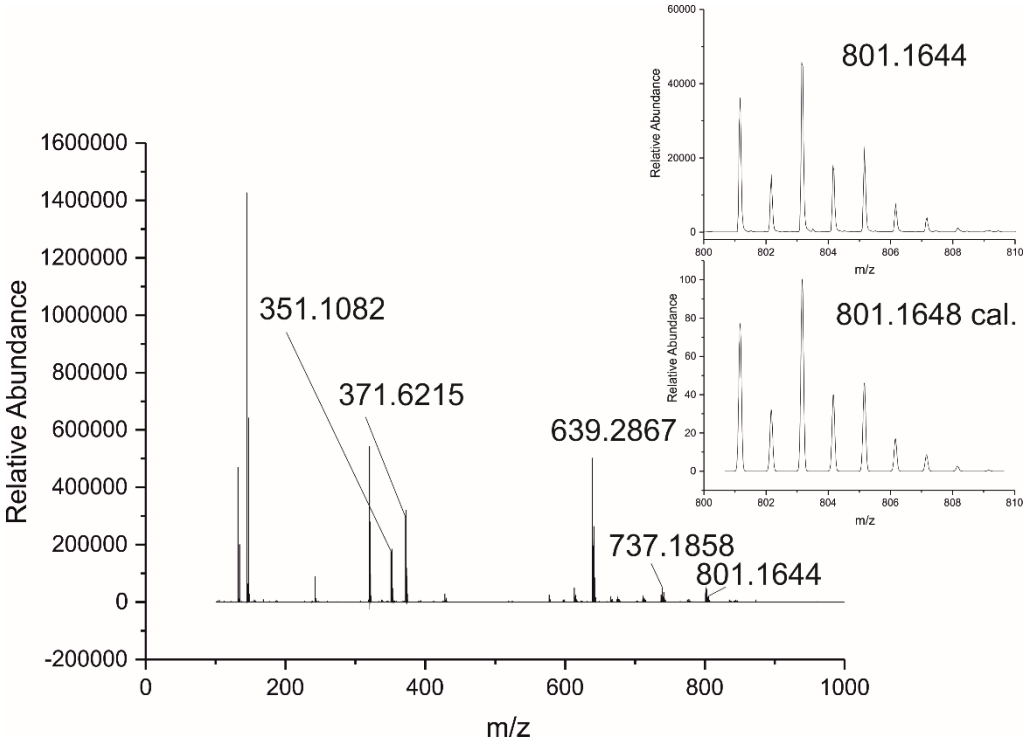

Figure S46. ESI-MS of **6** in acetonitrile. The inserted graphs show the measured (top) and calculated (below) isotopic pattern for the peak at m/z = 801.1644 corresponding to $[(\mathbf{L^1})(Cu)_2{+}ClO_4]^+$.

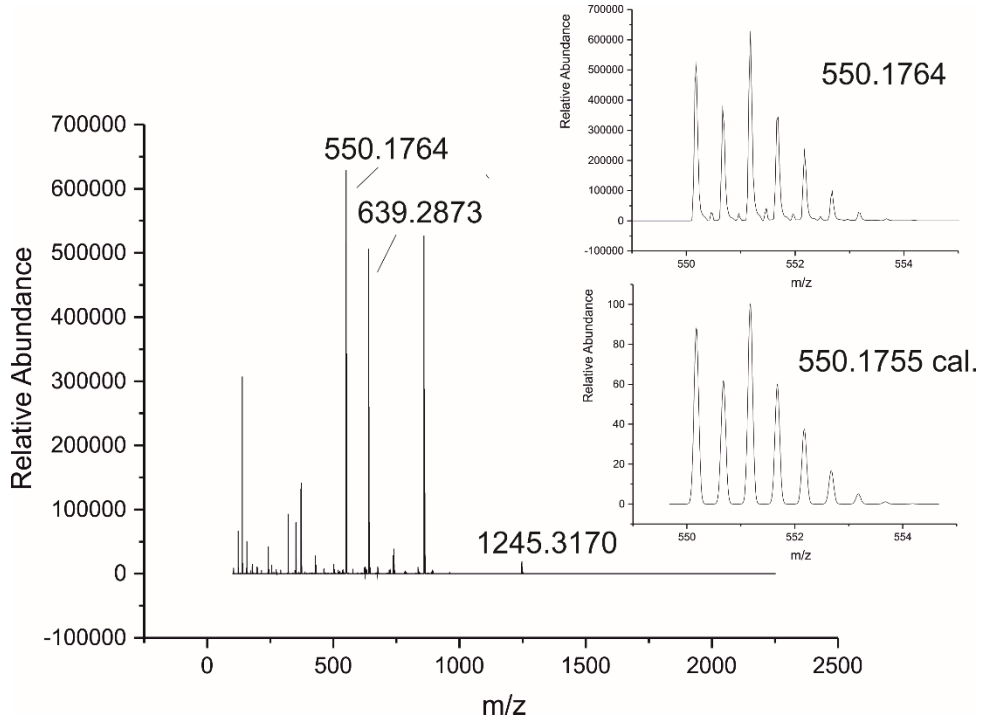

Figure S47. ESI-MS of **7** in acetonitrile. The inserted graphs show the measured (top) and calculated (below) isotopic pattern for the peak at m/z = 550.1764 corresponding to $[(\mathbf{L^1})(Cu)_2dppe]^{2+}$.

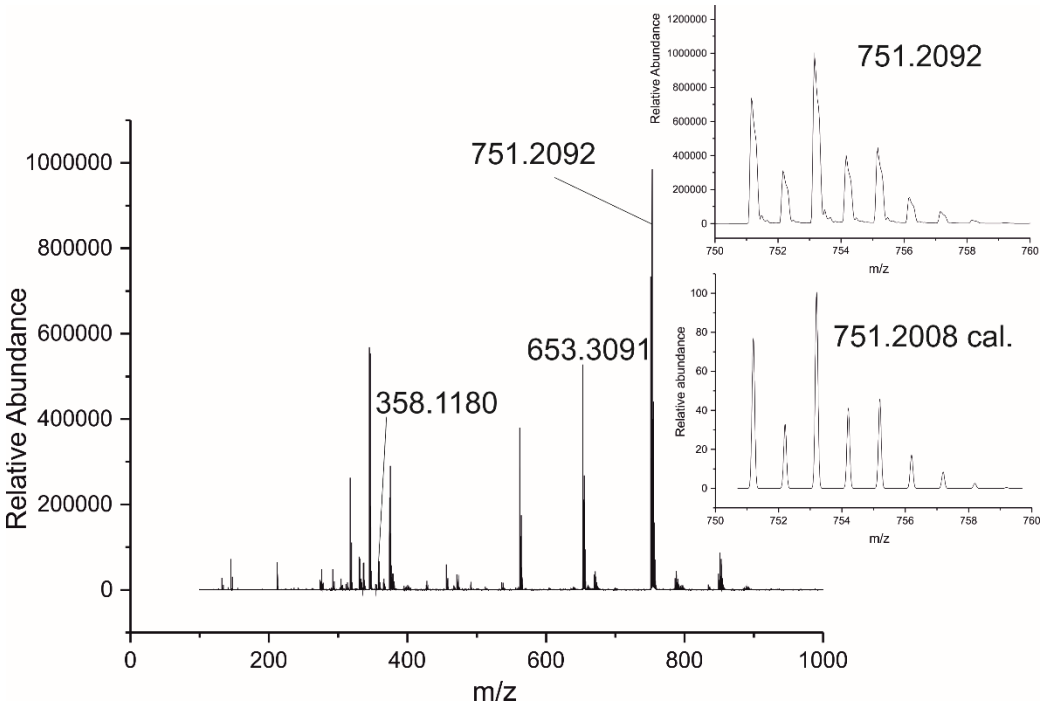

Figure S48. ESI-MS of **8** in acetonitrile. The inserted graphs show the measured (top) and calculated (below) isotopic pattern for the peak at m/z = 751.2092 corresponding to $[(\mathbf{L^2})(Cu)_2Cl]^+$.

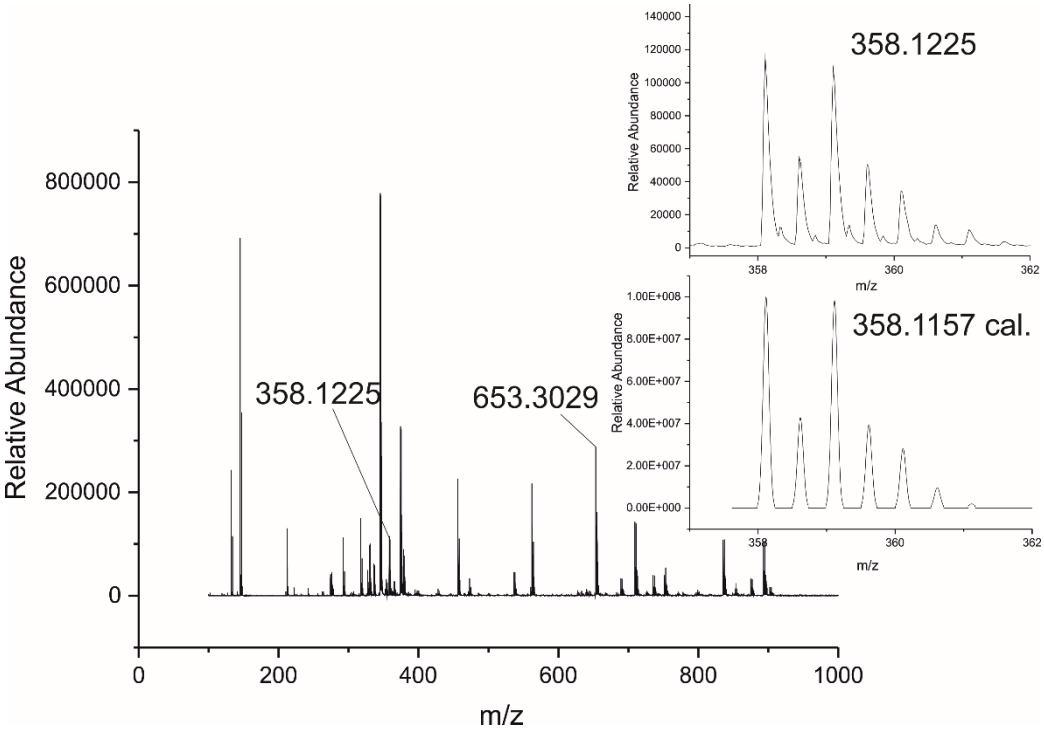

Figure S49. ESI-MS of **9** in acetonitrile. The inserted graphs show the measured (top) and calculated (below) isotopic pattern for the peak at m/z = 358.1225 corresponding to $[(\mathbf{L^2})(Cu)_2]^{2+}$.

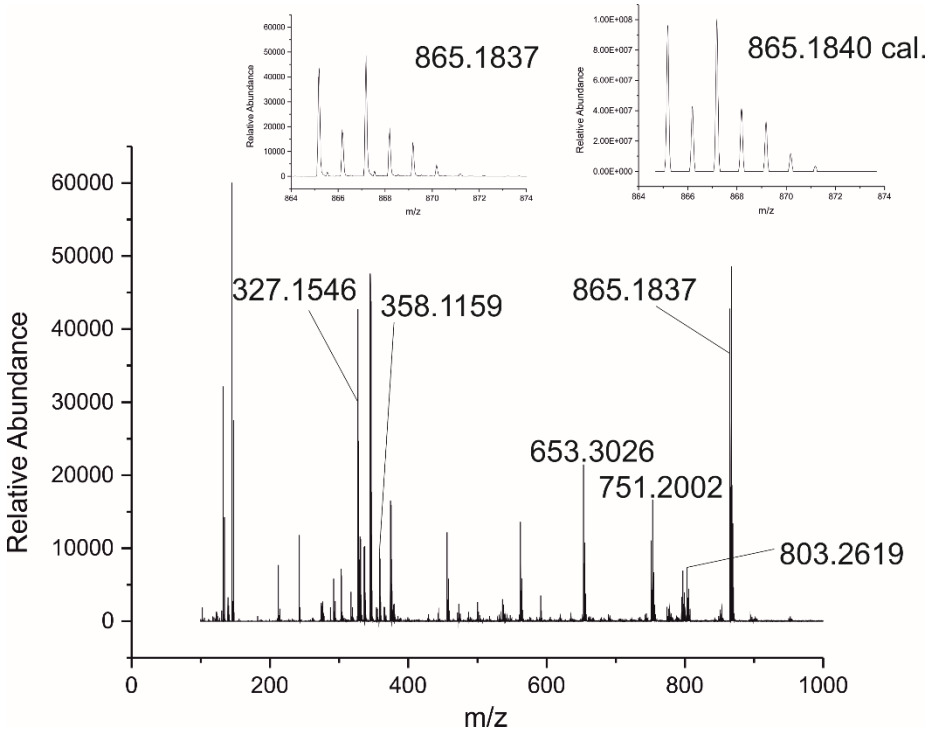

Figure S50. ESI-MS of **10** in acetonitrile. The inserted graphs show the measured (left) and calculated (right) isotopic pattern for the peak at m/z = 865.1837 corresponding to $[(\mathbf{L^2})(Cu)_2OTf]^+$.

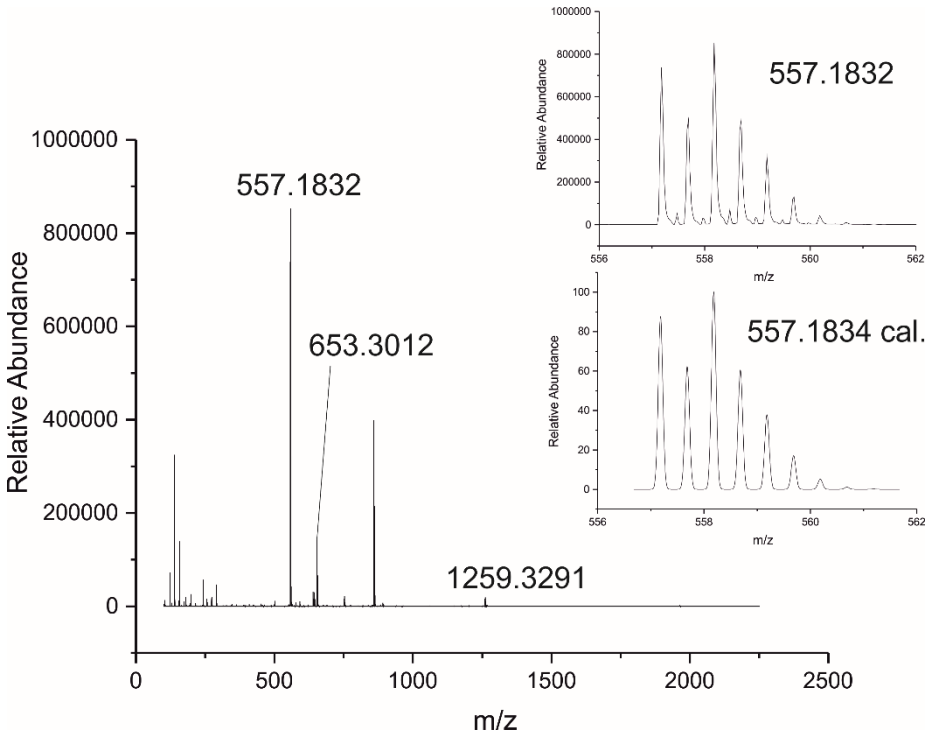

Figure S51. ESI-MS of **11** in acetonitrile. The inserted graphs show the measured (top) and calculated (below) isotopic pattern for the peak at m/z = 557.1832 corresponding to $[(\mathbf{L^2})(Cu)_2dppe]^{2+}$.

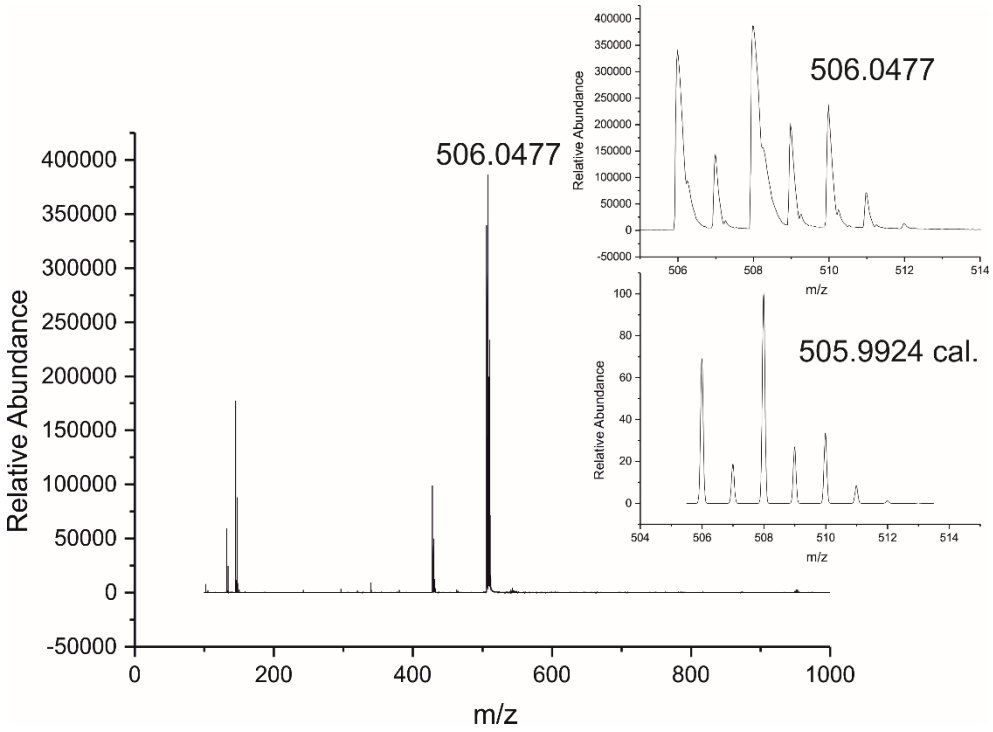

Figure S52. ESI-MS of **12** in acetonitrile. The inserted graphs show the measured (top) and calculated (below) isotopic pattern for the peak at m/z = 506.0477 corresponding to [(**DBF-BrNPy$_2$**)(Cu)]$^+$.

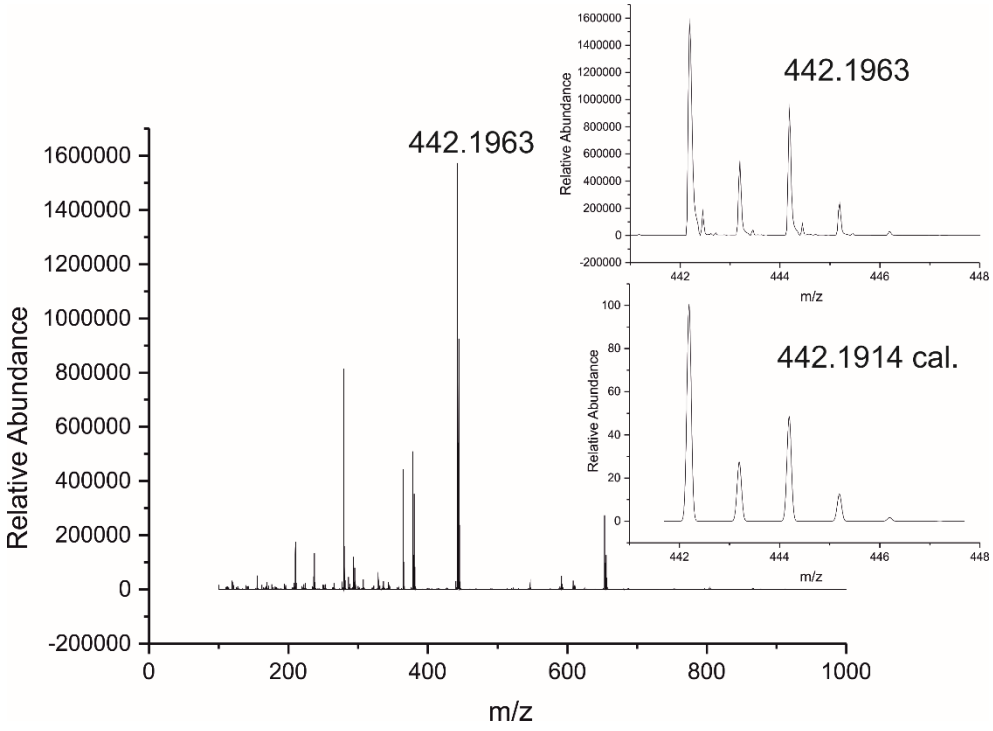

Figure S53. ESI-MS of **13** in acetonitrile. The inserted graphs show the measured (top) and calculated (below) isotopic pattern for the peak at m/z = 442.1963 corresponding to [(**DBF-HTacn**)(Cu)]$^+$.

4. UV/Vis spectra

4.1 Formation of the O adduct of 4, 6 and 10

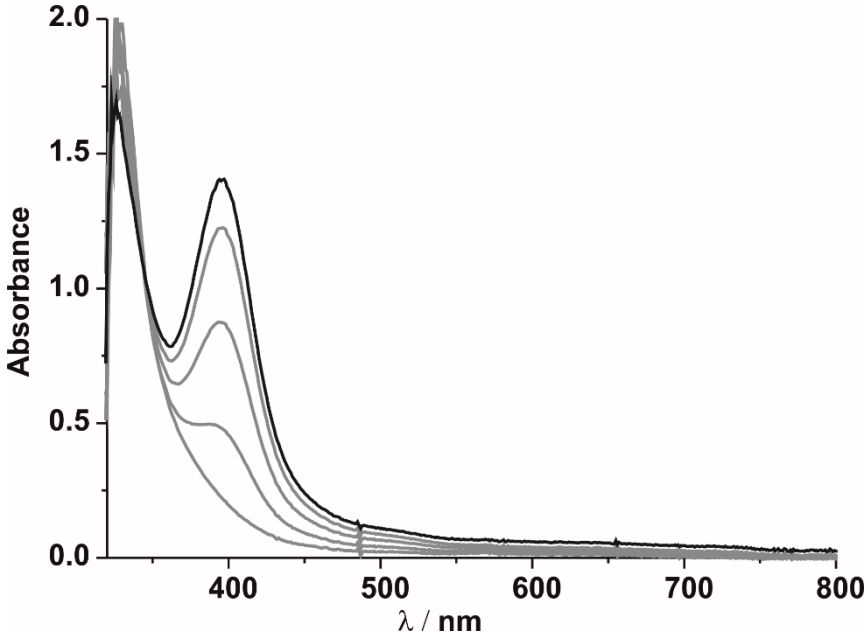

Figure S54. UV/Vis absorption spectra for the reaction of **4** (0.25 mM) with O_2 in acetone at -90 °C. The different graphs represent the spectra recorded 1, 80, 190, 30, 420 and 730 s after the injection of **4** (dissolved in 0.2 mL acetone) into an oxygen-saturated dry acetone solution (2.8 mL), respectively.

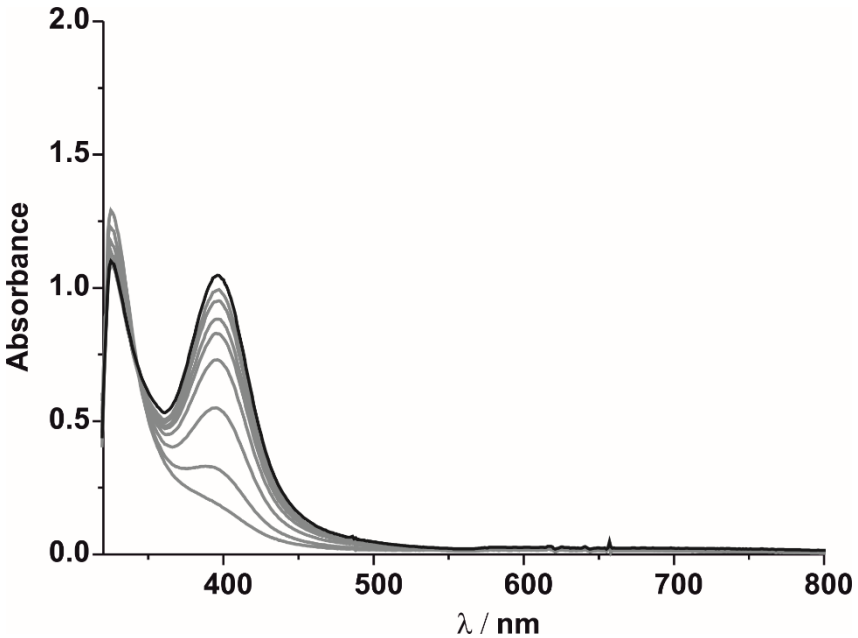

Figure S55. UV/Vis absorption spectra for the reaction of **6** (0.18 mM) with O_2 in acetone at -90 °C. The different graphs represent the spectra recorded 1, 5, 15, 30, 45, 60, 90, 120 and 250 s after the injection of **6** (dissolved in 0.2 mL acetone) into an oxygen-saturated dry acetone solution (2.8 mL), respectively.

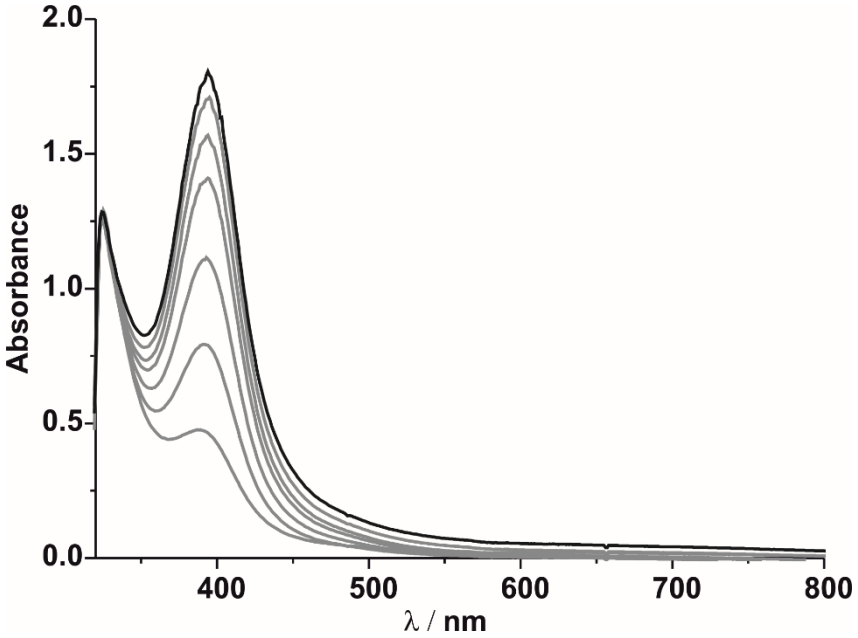

Figure S56. UV/Vis absorption spectra for the reaction of **10** (0.18 mM) with O_2 in acetone at -90 °C. The different graphs represent the spectra recorded 4, 8, 14, 24, 34, 54 and 88 s after the injection of **10** (dissolved in 0.2 mL acetone) into an oxygen-saturated dry acetone solution (2.8 mL), respectively.

4.2 Kinetic studies on the oxidation of exogenous substrates

To investigate the potential of the **O** adduct of **5** or **9** to perform oxidation reactions, the formed **O** adduct was treated with organic substrates and the reaction was monitored by UV/Vis spectroscopy. We observed that under conditions of excess substrate the absorption band at 393 nm or 396 nm characteristic for the **O** adduct of **5** or **9** decay immediately after addition of xanthene (20 equiv.), 2,4-di-*tert*-butylphenol (5 equiv.) and sodium 2,4-di-*tert*-butylphenolate (5 equiv.). Same observation were made for the **O** adduct of **5** after addition of PPh_3 (20 equiv.).

No faster decay of the band at 393 nm or 396 nm could be observed compared to the self decay of the **O** adducts of **5** or **9** for the addition of an excess of ethylbenzene (100 equiv.) or benzoylchloride (100 equiv.).

For the addition of 4-methoxybenaldehyde (20, 30, 40 50 equiv. for the **O** adduct of **5** and 50, 100, 150, 200 equiv. for the **O** adduct of **9**) the band at 393 nm or 396 nm decayed following an exponential curve. This is also the case for the addition of PPh_3 (50, 100, 150, 200 equiv.) to the **O** adduct of **9**. The pseudo-first order kinetics could be fitted to monoexponential functions, from which observed rate constants (k_{obs}) could be extracted. The rate constants k_{obs} were found to be linearly increasing with the increment of substrate concentrations. The slope of the rate constant (k_{obs}) versus substrate concentration fitting plot provided the second order rate constants (k_2).

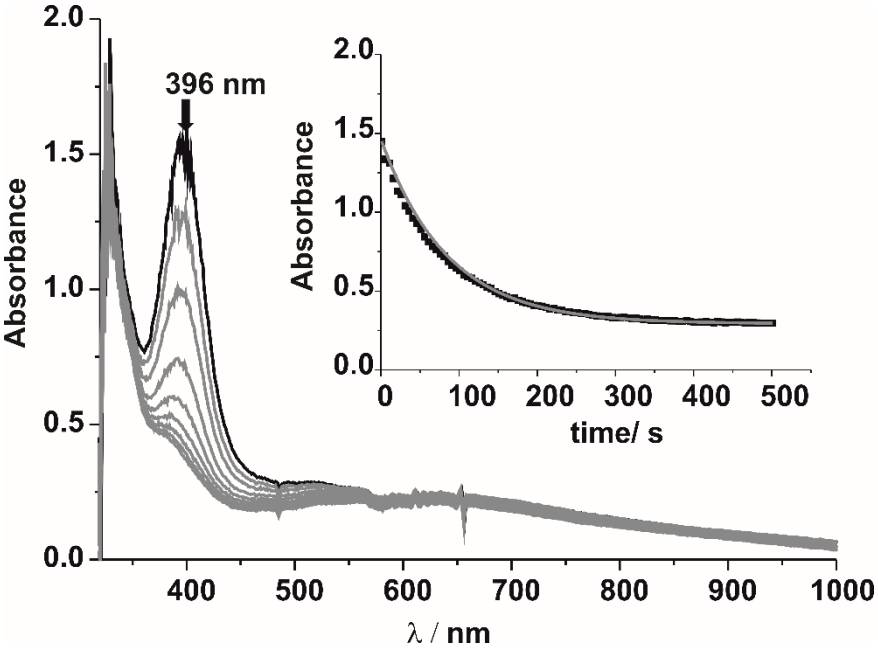

Figure S57. Changes in the absorption spectra of the **O** adduct of **5** (0.18 mM) with 4-methoxybenaldehyde (20 equiv.) in acetone at −90 °C. The inset shows the pseudo-first order decay of the 396 nm absorption band as a function of time upon addition of 4-methoxybenzaldehyde ($k_{obs} = 1.38 \cdot 10^{-2}$ s^{-1}).

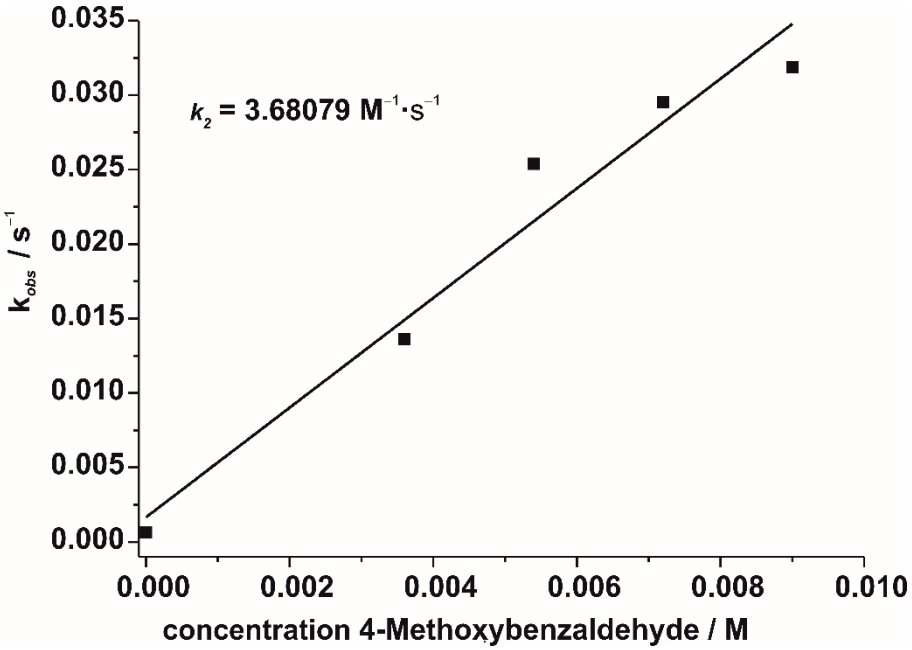

Figure S58. k_{obs} measured at different 4-Methoxybenzaldehyde concentrations in acetone at −90 °C.

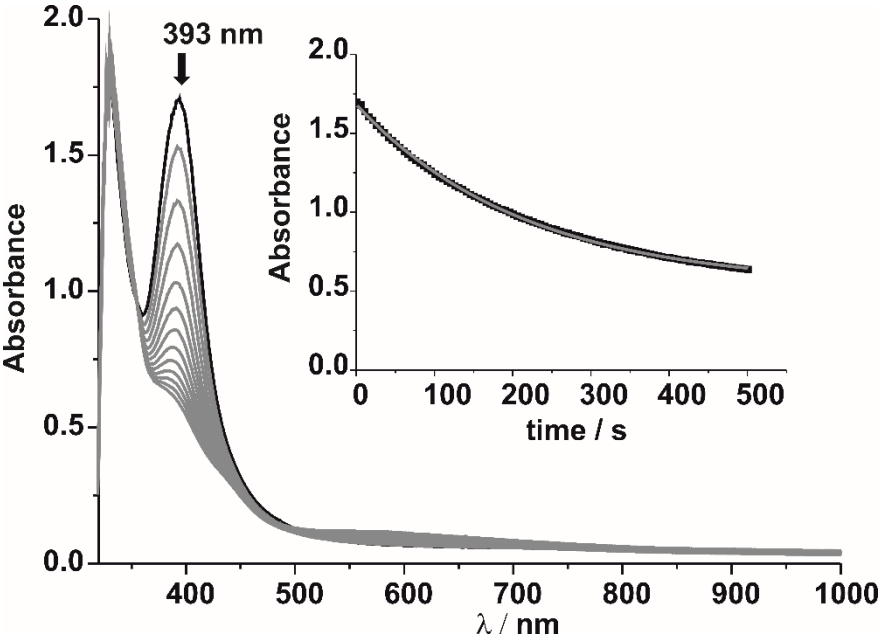

Figure S59. Changes in the absorption spectra of the **O** adduct of **9** (0.18 mM) with 4-methoxybenaldehyde (50 equiv.) in acetone at –90 °C. The inset shows the pseudo-first order decay of the 393 nm absorption band as a function of time upon addition of 4-methoxybenzaldehyde ($k_{obs} = 4.88 \cdot 10^{-3}$ s^{-1}).

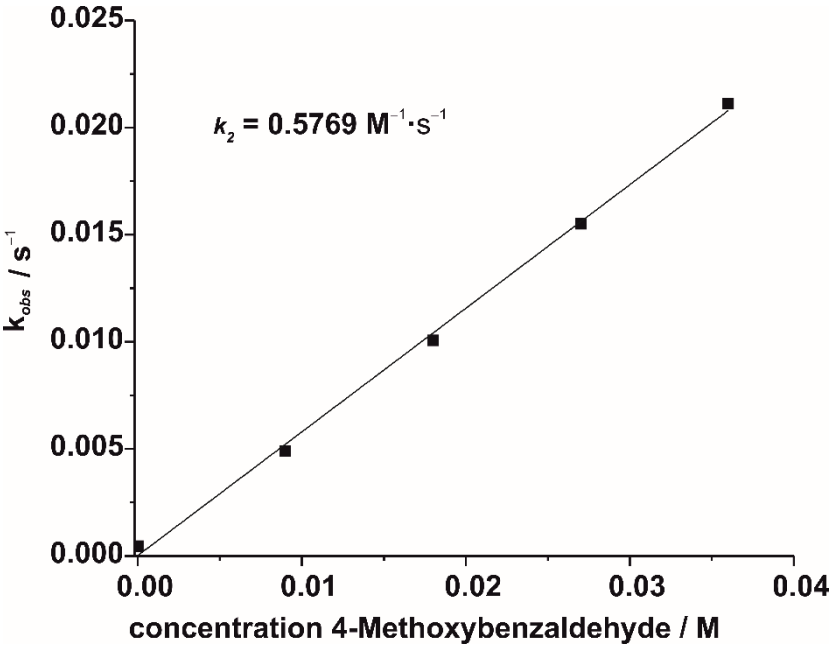

Figure S60. k_{obs} measured at different 4-Methoxybenzaldehyde concentrations in acetone at –90 °C.

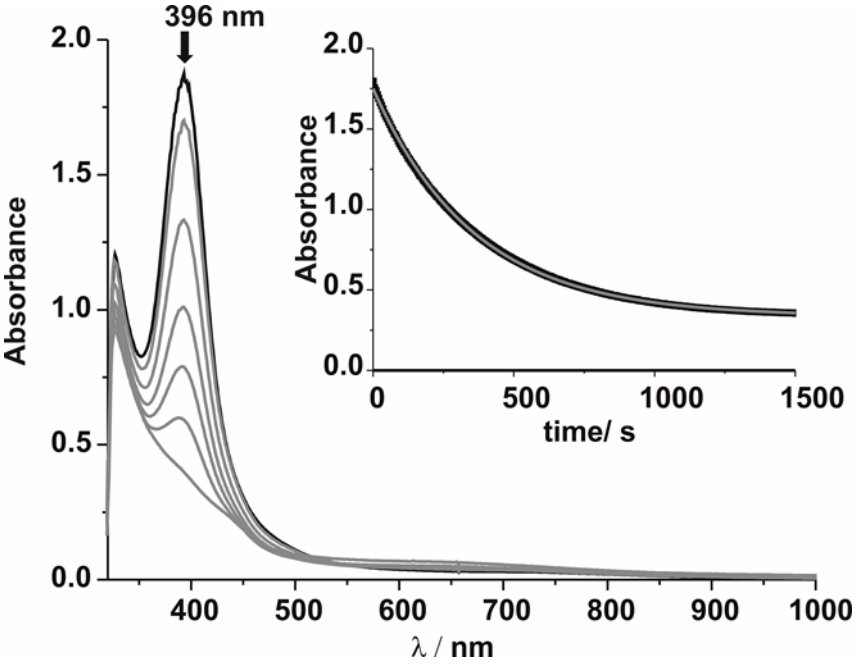

Figure S61. Changes in the absorption spectra of the **O** adduct of **9** (0.18 mM) with Triphenylphosphine (100 equiv.) in acetone at –90 °C. The inset shows the pseudo-first order decay of the 396 nm absorption band as a function of time upon addition of Triphenylphosphine ($k_{obs} = 2.18 \cdot 10^{-3}$ s^{-1}).

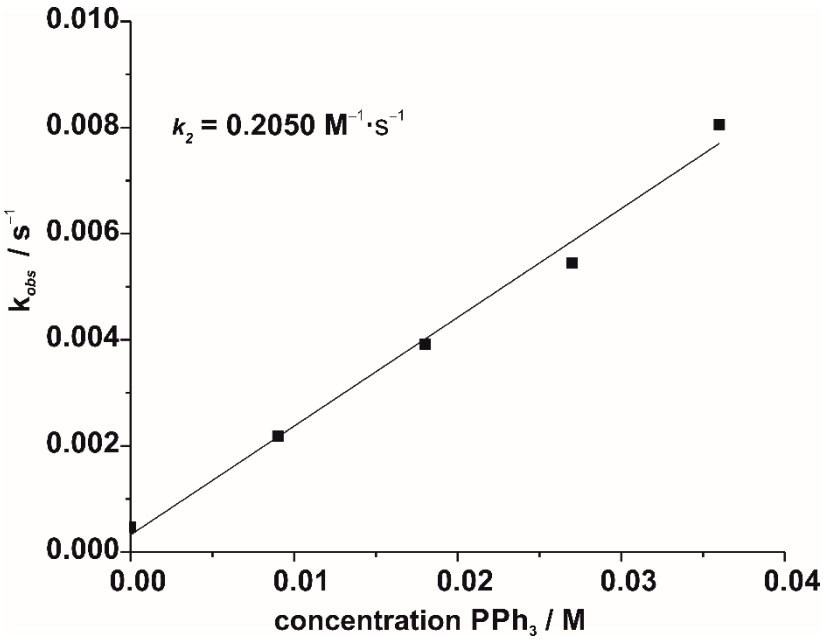

Figure S62. k_{obs} measured at different triphenylphosphine concentrations in acetone at –90 °C.

Table S3. Reactivity of the **O** adducts of **5** or **9**. The yields are based on the used amount of the respective starting complex **5** or **9**.

Substrate	Products for **O** adduct of **5**	k_2	Products for **O** adduct of **9**	k_2
PPh_3	PPh3=O (94 %)	[a]	PPh3=O (90 %)	0.2050 $M^{-1}\cdot s^{-1}$
Xanthene	Xanthone (92 %)	[a]	Xanthone (>95 %)	[a]
2,4-Di-*tert*-butylphenol	3,3´,5,5´-Tetra-*tert*-butyl-2,2'-bis(phenol) (43 %)	[a]	3,3´,5,5´-Tetra-*tert*-butyl-2,2'-bis(phenol) (41 %)	[a]
Sodium 2,4-di-*tert*-butylphenolate	3,3´,5,5´-Tetra-*tert*-butyl-2,2'-bis(phenol) (81 %)	[a]	3,3´,5,5´-Tetra-*tert*-butyl-2,2'-bis(phenol) (73 5 %)	[a]
4-Methoxy-benzaldehyde	4-Methoxy benzoic acid (> 95 %)	3.68079 $M^{-1}\cdot s^{-1}$	4-Methoxy benzoic acid (86 %)	0.5769 $M^{-1}\cdot s^{-1}$

[a] Reaction too fast for kinetic studies.

5. References

1 a) Sheldrick, G. M. Acta Crystallogr., Sect. A 2008, 64, 112–122; b) Sheldrick, G. M. SHELXL-2013, Program for Crystal Structure Refinement, University of Göttingen, Germany, 2013

2 Sheldrick, G. M. SADABS, University of Göttingen, Germany, 1996